EUROPEAN ORGANIZATION FOR NUCLEAR RESEARCH

CERN-EP/83-185
5 December 1983

A SPIN-PARITY ANALYSIS OF THE $\omega\pi^0$ ENHANCEMENT PHOTOPRODUCED IN THE ENERGY RANGE 20 TO 70 GeV

Bonn[1]-CERN[2]- Glasgow[3]-Lancaster[4]-Manchester[5]-
Paris VI[6]- Rutherford[7]-Sheffield[8]

M. Atkinson[7], T.J. Axon[5], D. Barberis[5], T.J. Brodbeck[4], G.R. Brookes[8], J.J. Bunn[8], P.J. Bussey[3], A.B. Clegg[4], J.B. Dainton[3], M. Davenport[7], B. Dickinson[5], B. Diekmann[1], A. Donnachie[5], R.J. Ellison[5], P. Flower[7], P.J. Flynn[4], W. Galbraith[8], K. Heinloth[1], R.C.W. Henderson[4], R.E. Hughes-Jones[5], J.S. Hutton[7], M. Ibbotson[5], H.P. Jakob[1], M. Jung[1], M.A.R. Kemp[7], B.R. Kumar[7], J. Laberrigue[6], G.D. Lafferty[5], J.B. Lane[5], J.C. Lassalle[2], J.M. Levy[6], V. Liebenau[1], R.H. McClatchey[8], D. Mercer[5], J.A.G. Morris[7], J.V. Morris[7], D. Newton[4], C. Paterson[3], G.N. Patrick[2], E. Paul[1], C. Raine[3], M. Reidenbach[1], H. Rotscheidt[1], A. Schlösser[1], P.H. Sharp[7], I.O. Skillicorn[3], K.M. Smith[3], K.M. Storr[2], R.J. Thompson[5], Ch. de la Vaissière[6], A.P. Waite[5], M.F. Worsell[5] and T.P. Yiou[6]

(The Omega Photon Collaboration)

ABSTRACT

A study is made of the $\omega\pi^0$ system produced near threshold in the reaction $\gamma p \to \pi^+\pi^-\pi^0\pi^0 p$. A spin-parity analysis shows that the $\omega\pi^0$ enhancement is consistent with predominant 1^+ B(1235) production, with $\sim$ 20% $J^P = 1^-$ background.

(Submitted to Nuclear Physics B)

1. INTRODUCTION

Radial recurrences of the ρ meson are predicted by both the quark model [1] and by duality arguments [2]. To date the only identified recurrence of the ρ is the $\rho'(1600)$ [3]. However the quark model with an effective scalar confining potential would predict the first recurrence at a mass of ∿ 1.3 GeV [1]. A candidate for this state is the $\omega\pi^0$ enhancement of mass ∿ 1.25 GeV which has been observed in photoproduction experiments [4,5] in the channel

$$\gamma p \rightarrow \pi^+\pi^-\pi^0\pi^0 p \ . \qquad (1)$$

Attempts have been made to determine the spin-parity $\left(J^P\right)$ of this enhancement, but owing to lack of statistics this has been possible only by assuming s-channel helicity conservation (SCHC) in the production mechanism [5]. With this assumption the favoured J^P was 1^-.

In this experiment we make a J^P analysis without the assumption of SCHC. We find that the enhancement is consistent with the predominant production of the B(1235) meson by a mechanism which does not conserve s-channel helicity.

2. EXPERIMENTAL SET-UP AND DATA SELECTION

An 80 GeV electron beam from the CERN Super Proton Synchrotron (SPS) was used to generate partially plane polarized photons by coherent bremsstrahlung in a silicon crystal [6,7]. These photons were tagged in the energy range 20-70 GeV. The distributions of incident photon energy and polarization intensity (calculated as described in ref. 7) are shown in fig. 1. The photon energy spectrum was determined by using a subsidiary unbiased trigger which required only a signal from an end-cap scintillation counter immediately following the hydrogen target (fig. 2). Approximately half of the data were taken with the plane of polarization at +45° to the median plane of the Omega spectrometer, and half at -45°. (These are labelled as negative and positive values of polarization, P_γ, in fig. 1b.) The mean polarization, averaged over the photon energy spectrum, was 0.30.

Photons entered the Omega spectrometer which contained a 60 cm liquid hydrogen target, multiwire proportional chambers (MWPCs) and, downstream of the magnet, drift chambers, a threshold Cherenkov counter and a photon calorimeter. The layout is shown in fig. 2, and has been described elsewhere [8].

The photon calorimeter comprised an active converter (sampler) made up of 42 slabs of lead glass, each of three radiation lengths in depth, followed by a shower position detector hodoscope (Penelope) of 792 scintillation counters and finally an array of 343 lead-glass blocks (Olga), each of area 140 × 140 mm^2 and depth 500 mm ($\sim$ 20 radiation lengths). The calorimeter subtended a solid angle of 0.07 sr about the forward direction, and measured the photon direction to an accuracy of $\pm$0.2 mrad, with an energy resolution $\delta E/E \sim 10\%/\sqrt{E}$.

Events from reaction (1) were selected by a trigger which required between two and five forward charged particles plus a signal from the photon calorimeter indicating the detection of at least one γ-ray of energy above 2 GeV. Electromagnetic background was reduced by a system of veto counters in the median plane, consisting of the median row blocks of the lead-glass array plus additional electron veto counters (EVAs) (see fig. 2). Pattern recognition and geometrical reconstruction of events were performed by the program TRIDENT [9]. A second program reconstructed the momentum and polarization of the incident photons, decoded the Cherenkov information for particle identification, and reconstructed γ-rays and π^0 mesons.

Channel (1) was selected by requiring a well-measured beam photon, two π^0's, and two or three charged particles consistent with being $\pi^+\pi^-$ or $\pi^+\pi^-$p, which were reconstructed to a single vertex in the hydrogen target.

From the interaction of 5.6×10^{10} photons with the 2.54×10^{24} protons/cm^2 of the hydrogen target, a total of $\sim$ 20,000 candidates for reaction (1) were obtained. Figure 3a shows the distribution of missing mass squared opposite the $\pi^+\pi^-\pi^0\pi^0$ for all candidate events. Final selection of channel (1) required the missing mass squared to be in the range -2.1 GeV^2 to +3.9 GeV^2, giving a sample of 8100 events.

Selection of the channel

$$\gamma p \to \omega\pi^0 p \qquad (2)$$

requires selection of ω events free from background. To do this, weights were assigned to each $\pi^+\pi^-\pi^0$ combination according to the 3π mass (fig. 4) as follows:

for $0.733 < m_{3\pi} < 0.833$ (the ω-peak region)	weight = +1 ,
for $0.683 < m_{3\pi} < 0.733$ and $0.833 < m_{3\pi} < 0.883$ (the ω-wings region)	weight = −1 ,
otherwise	weight = 0 .

In all subsequent analyses of channel (2), each 3π combination was used with the above weight. With this procedure the weighted number of $\omega\pi^0$ events was 2304. To show that this sample is free from background, we plot in fig. 5 the ω decay matrix element squared (λ):

$$\lambda = |\vec{p}_+ \times \vec{p}_-|^2 / |\vec{p}_+ \times \vec{p}_-|^2_{max} ,$$

where $\vec{p}_+$ and $\vec{p}_-$ are the three-momentum vectors of the π^+ and π^- in the 3π rest frame. As expected the signal in the ω-peak region rises linearly with λ, whereas it is flat in the ω-wings region. This shows that the background subtraction method described above does select a pure sample of ω events.

The missing mass squared opposite the $\omega\pi^0$ is shown in fig. 3b, indicating $\sim$ 15% background from inelastic $\omega\pi^0$ production.

3. ACCEPTANCE

In order to correct the observed angular distributions for experimental bias, we have used a detailed Monte Carlo simulation of the acceptance [10].

Events of channel (2) were generated [11] with a photon bremsstrahlung spectrum as determined by the monitor trigger described above (fig. 1a). The production cross-section was taken to be independent of energy, and the differential cross-section, $d\sigma/dt$, was assumed exponential with a slope of 5 GeV^{-2}.

These events were then passed through the acceptance simulation [10], which included the multiplicity requirements of the trigger, the geometrical cuts imposed

by the apparatus, chamber inefficiencies, and showering of photons in the calorimeter. Accepted events were then processed using the same analysis program as the data. More details about the acceptance corrections can be found in Appendix D.

4. RESULTS

a) Mass spectra and momentum transfer distribution

The $\pi^+\pi^-\pi^0\pi^0$ and $\pi^+\pi^-\pi^0$ mass spectra are shown in figs. 6 and 4, respectively. The $\pi^+\pi^-\pi^0\pi^0$ spectrum shows enhancements at $\sim$ 1.25 and 1.6 GeV. The 1.6 GeV enhancement has been described elsewhere [12]. The $\pi^+\pi^-\pi^0$ spectrum shows a strong ω signal of FWHH $\sim$ 35 MeV over a background of $\sim$ 20%. This background was removed by the peak-wings subtraction described in section 2, and the resulting $\omega\pi^0$ mass spectrum is shown (shaded) in fig. 6. Evidently the 1.25 enhancement decays primarily into $\omega\pi^0$.

The four-momentum transfer squared (t) distribution is shown in fig. 7, and is consistent with a peripheral production mechanism, with $d\sigma/dt \sim e^{5t}$.

b) Decay angular distributions

The decay of the $\omega\pi^0$ system can be described in terms of the following four angles (Appendix A): θ and ϕ are the polar and azimuthal angles (Ω) of the ω in the $\omega\pi^0$ s-channel helicity frame; θ_H and ϕ_H are the polar and azimuthal angles (Ω_H) of the normal to the ω decay plane in the ω helicity frame [13].

The decay angular distribution has been analysed in terms of 25 orthogonal functions [13], or moments, $H^{\pm}_{\ell mLM}(\Omega,\Omega_H)$, which form a complete set for the description of angular distributions arising from $\omega\pi^0$ spin-parities 0^-, 1^-, and 1^+ (see table 1 and Appendix B). By summing these moments over all events, and correcting the resulting sums for the effects of acceptance by using a linear algebra technique [14], the angular decay distribution can be obtained (Appendix D):

$$W(\Omega,\Omega_H) = \sum_{\alpha} H^{\pm}_{s}(\alpha) H^{\pm}_{\alpha}(\Omega,\Omega_H)/C_{\alpha} \qquad \alpha \equiv \ell mLM \ .$$

The corrected moment sums $H^{\pm}_{s}(\alpha)$ are directly related to the relative intensities in each J^P state, the production density matrix, and the decay amplitudes

(table 2, Appendix C). The experimental distributions of the $\omega\pi^0$ decay angles, for all events, are shown in fig. 8 and the moment sums, corrected for acceptance, $[NH_s^0(\alpha)$, see eqns. D15 and D7$]$ are shown in fig. 9 as a function of $\omega\pi^0$ mass.

To check that the 25 moments used in the analysis do provide a complete description of the $\omega\pi^0$ angular distributions, we have used the corrected distribution $W(\Omega,\Omega_H)$ as input to the acceptance simulation to produce the smooth curves in fig. 8. Evidently the curves give a good description of the data showing that the 25 moments used are sufficient, and that there is no need to consider higher spin states of the $\omega\pi^0$ system.

c) Spin-parity analysis

An examination of the $\omega\pi^0$ mass spectrum (fig. 6) suggests that it can be interpreted as a resonant state of mass $\sim$ 1.2 GeV and width $\sim$ 200 MeV plus $\sim$ 20% background. If this is the case, we expect one spin-parity state to dominate and to determine the form of the angular distributions shown in fig. 8.

Acceptance calculations show that, in contrast to θ, the angles ϕ, θ_H, and ϕ_H are not strongly biased, and can thus be interpreted directly in terms of spin-parity states. The distribution $\cos\theta_H$ shows a strong $\sin^2\theta_H$ component, indicating a significant contribution from ω helicity = ±1. Thus the dominant spin-parity cannot be 0^-, since this produces ω helicity = 0. A dominant 1^+ state could account for this distribution with a suitable (non-zero) choice for the D/S ratio in the decay amplitude. A 1^- state can only produce ω helicity = ±1 and could account for the $\sin^2\theta_H$ component provided that the background is mainly ω helicity = 0 (i.e. 0^- and/or 1^+). The ϕ_H distribution shows a strong $\cos 2\phi_H$ component, as expected for a SCHC 1^- state. An SCHC 1^+ state would produce a $\sin 2\phi_H$ component, so if the dominant state is 1^+ it must be produced by a non-SCHC mechanism with $\rho^0_{00} > 1/3$. The ϕ distribution shows a $\sin\phi$ component, which can only arise from interference between $\omega\pi^0$ helicities ±1 and 0 (Re $\rho^0_{10} \neq 0$), thus showing that there is a non-SCHC component to the production mechanism. However, without further analysis, we cannot determine whether the non-SCHC states are associated with the signal or with the background.

In summary, from the projected angular distributions, we rule out 0^- as the dominant spin-parity, but cannot distinguish between SCHC 1^- and non-SCHC 1^+. To proceed further we have made a detailed spin-parity analysis by taking into account the correlations between the angles θ, ϕ, θ_H, and ϕ_H. This was done by fitting [15] the acceptance corrected moment sums using the expressions given in table 2, to obtain the intensities in each J^P state, the density matrix elements*), and the D/S ratio for the 1^+ state.

Fits were made to the moment sums over the whole $\omega\pi^0$ mass range, the data being divided into nine bins of 100 MeV width between 0.9 GeV and 1.8 GeV. In the first fit made (Fit 1) no restrictions were imposed and all three spin-parity states were allowed. This gave 17 free parameters and 25 measured moment sums in each mass bin; the results are shown in fig. 10. In general the fits gave good values of χ^2. We make the following observations: the amount of 0^- required by the fits was small, and consistent with zero across the mass range; the amounts of 1^+ and 1^- were, within large errors, equal; in general, the errors on all fitted variables were large and, in addition, the variables were strongly correlated. In principle the distributions of θ and ϕ should allow the 1^+ (S + D wave) component to be distinguished from 1^- and 0^- (P wave). However, the strong acceptance correction in the θ distribution means that the statistical errors on this distribution are large, so that most of the information comes from the ϕ, θ_H, and ϕ_H correlations. As has already been noted, the relative amounts of ω helicity (± 1 0) can be represented by a 1^+ state with suitable D/S ratio, or by a combination of 1^- and 0^-, so that the θ_H and ϕ_H distributions cannot distinguish between these two possibilities. This accounts for the large uncertainty in the relative amounts of 1^+

---

*) The density matrix elements in table 2, which are extracted by the fits are the measurable quantities

$$\mathrm{Re}\left\{\rho^{ij}_{\Lambda\Lambda'} e^{i\phi_{ij}}\right\},$$

where i(j) are the states concerned, and ϕ_{ij} is the difference in decay phase. For the diagonal terms this reduces to

$$\mathrm{Re}\left\{\rho^{ii}_{\Lambda\Lambda'}\right\}.$$

and 1^- as determined by Fit 1, and in order to progress beyond this we have to introduce some additional constraint.

Since Fit 1 indicates that the 0^- intensity is small, and this state cannot be diffractively photoproduced, we have performed a second fit (Fit 2, fig. 11), where the 0^- intensity has been fixed at zero. Again this fit gave acceptable values of χ^2 across the mass range, but in this case the amount of 1^+ was increased in the region of 1.2 GeV compared with Fit 1. The 1^- state is consistent with SCHC, within errors (ρ^0_{00} = Re ρ_{10} = ρ_{1-1} = 0).

Since the 1^- state is consistent with being SCHC, a third fit has been made (Fit 3) in which we have constrained the 1^- state to be SCHC; the results are shown in fig. 12. These are consistent with Fit 2, with reduced errors on the fitted parameters, and lead to the following conclusions: the 1^+ intensity peaks at $\sim$ 1.2 GeV with a full width of $\sim$ 200 MeV and is approximately four times the 1^- intensity; the D/S ratio in the peak is $\sim$ 0.25, and $\rho_{00} \sim 0.4$ across the mass range. Thus the 1^+ state is consistent with the B(1235) meson, but is not produced by an SCHC mechanism. The 1^- intensity shows no evidence for an enhancement. The density matrix elements for the interference between the 1^+ and 1^- states (ρ_{11}, ρ_{01}, ρ_{1-1}) show no strong dependence on $\omega\pi^0$ mass.

To check the consistency of the data with an interpretation in terms of the B(1235) meson and a $J^P = 1^-$ background, and to impose continuity as a function of $\omega\pi^0$ mass on the fitted parameters, we have made a series of model dependent fits. These fits were made to all of the mass bins (i.e. to $9 \times 25 = 225$ measured moment sums) with a resonant parametrization for the 1^+ decay amplitude, and allowing the relative production phase of the 1^+ and 1^- states to vary (see Appendix E). Two types of fit were made, allowing the 1^- state to be either resonant or non-resonant.

In parametrizing the non-resonant 1^- state we have tried two different methods: i) as the tail of the $\rho^0(770)$ decaying into $\omega\pi^0$ [16], ii) as a Weibull function [17] with the decay phase independent of $\omega\pi^0$ mass. For the widths of the resonant states,

we have tried both mass dependent and mass independent forms (if the 1^+ state is the B(1235), with $\sim$ 100% branching ratio to $\omega\pi^0$ we expect a strongly mass dependent width, since the resonance is close to $\omega\pi^0$ threshold).

All fits gave equally good descriptions of the data with χ^2 of $\sim$ 290. In particular, the form of the interference moments $[H_s^-(\ell mLM)]$ can be fitted equally well with either a resonant or non-resonant 1^- state by changing the relative production phase of the 1^- state with respect to the 1^+ state. The results of the fit for which the 1^- state has been parametrized as the tail of the $\rho^0(770)$ are shown in table 3, and by the dashed curves of fig. 9.

The characteristics found for the 1^+ state show only small systematic variations with the different parametrizations outlined above, and are consistent with the results of the model independent Fit 3. The intensity and production characteristics of the 1^- state are similarly insensitive to parametrization, and are also consistent with Fit 3. In table 4 we list those results which are insensitive to the parametrization; the quoted systematic errors are estimated from the different fits.

To summarize these results, we find that the 1^+ state is dominant with a mass and D/S ratio consistent with the B(1235), but with a width of $\sim$ 230 MeV (220 MeV after correction for mass resolution) which is larger than found for the B meson. This width could be explained by $\sim$ 20% 1^+ S-wave background, as might be expected from a Deck mechanism [18], which would also decrease the observed D/S ratio (0.25 compared to 0.29 expected for the B meson). Other fits, allowing 0^- as either a resonant or non-resonant state, in addition to 1^+ and 1^- have been made; these fits gave results consistent with those described above.

d) Cross-section and production mechanism

As already shown, the t-distribution indicates a peripheral production mechanism with an exponential slope of 5.0 ± 0.3 GeV^2 (fig. 7), for reaction (2). Further information on the production mechanism can be obtained by studying the energy (E_γ) dependence of the total $\omega\pi^0$ cross-section. To do this, we have used the parametrization

$$\sigma(E_\gamma) = \sigma(39)\left(\frac{39}{E_\gamma}\right)^{\alpha} \mu b \qquad 20 \leq E_\gamma \leq 70 \text{ GeV} ,$$

to fit the energy dependence for reaction (2), with the results (39 GeV ≡ mean incident beam energy):

$$\sigma(39) = 0.86 \pm 0.27 \ \mu b$$

$$\alpha = 0.6 \pm 0.2 .$$

Corrections have been included for beam reconstruction efficiency, event reconstruction efficiency, $\omega \to \pi^+\pi^-\pi^0$ branching ratio, and hadronic interactions of the $\pi^\pm$ in the material of the spectrometer. The result, extrapolated to lower energies, is compared in fig. 13 with data from other experiments. Thus we conclude that the cross-section falls slowly with beam momentum, suggesting diffractive production.

The ratio $1^+:1^-$ at the peak in the 1^+ spectrum (Fit 3) is $\sim$ 8:2. When summed over the whole $\omega\pi^0$ mass range, the fraction of 1^+ is 73 ± 7%, giving a 1^+ cross-section of 0.63 ± 0.20 μb. If approximately 20% of this is due to background s-wave, the estimated cross-section $\sigma(\gamma p \to Bp) \sim 0.5$ μb.

Finally, the polarization moment sums $H_s^1(\ell mLM)$ have been fitted to determine the density matrix elements $\rho^1_{\Lambda\Lambda'}$ for the 1^+ and 1^- states (see Appendix D), and thus the parity asymmetry for each state [19]:

$$P_\sigma(1^-) = 2\rho^1_{1-1} - \rho^1_{00} = \frac{\sigma^N(1^-) - \sigma^U(1^-)}{\sigma^N + \sigma^U} ,$$

$$P_\sigma(1^+) = \rho^1_{00} - 2\rho^1_{1-1} = \frac{\sigma^N(1^+) - \sigma^U(1^+)}{\sigma^N + \sigma^U} ,$$

where σ^N and σ^U are the cross-sections for natural and unnatural parity exchange in the t-channel. However, the statistical errors on these quantities are large, and even if we constrain the 1^- to be produced by SCHC with natural parity exchange ($\rho^1_{1-1} = \frac{1}{2}$, all others = 0) we obtain

$$P_\sigma(1^+) = 0.3 \pm 0.7 ,$$

so that we cannot deduce the naturality of the exchange.

e) Comparison with other photoproduction reactions

Given the above estimate of the cross-section, $\sigma(\gamma p \to Bp)$, one can predict the photoproduction cross-sections for the other neutral, non-strange members of the $J^{PC} = 1^{+-}$ nonet, the H(1190) and H′ mesons. For ideal mixing, as in the case of the 1^{--} nonet, the cross-section ratios would be

$$\sigma(\gamma p \to Bp): \quad \sigma(\gamma p \to Hp): \quad \sigma(\gamma p \to H'p) \sim 9:1:2 ,$$

and the H′ would decay mainly into strange mesons. At the other extreme, for no mixing between the SU(3) octet and singlet, one would obtain

$$\sigma(\gamma p \to Bp): \quad \sigma(\gamma p \to Hp): \quad \sigma(\gamma p \to H'p) \sim 3:1:0 .$$

An analysis of $\pi^+\pi^-\pi^0$ photoproduction [20] has indicated a $J^{PC} = 1^{+-}$ enhancement in the $\rho\pi$ system whose parameters are compatible with the H(1190), and which is produced with a cross-section of about 300 nb. Also, in the study of $K\bar{K}\pi$ photoproduction [21] no evidence has been found for K*(890)K resonance production at the few nanobarn level. Taken together with our estimated B(1235) cross-section, both of these results indicate that the mixing angle in the $J^{PC} = 1^{+-}$ SU(3) multiplet must be small.

5. CONCLUSIONS

The data are consistent with non-SCHC production of the $J^P = 1^+$ B(1235) meson, together with a small S-wave 1^+ background as might be expected for a Deck mechanism. A small ($\sim$ 20%) $J^P = 1^-$ background, which conserves SCHC, is also present. This 1^- component is consistent with being due to the tail of the $\rho^0(770)$ decaying into $\omega\pi^0$. If $J^P = 0^-$ is allowed in addition to 1^+ and 1^-, a solution with roughly equal amounts of $J^P = 1^+$ and 1^- cannot be excluded unless the amplitudes are constrained in a model dependent way. The energy and t dependence of the $\omega\pi^0$ cross-section suggest a diffractive production mechanism.

Acknowledgements

We are grateful to the Omega group at CERN for their help in maintaining and running the spectrometer and providing on-line and off-line software. The work of the technical support staff in our home institutions, the support at the computer centres at Rutherford Appleton Laboratory, CERN, and the RHRZ at Bonn have been invaluable. We thank the SERC (UK), the BMFT (Fed. Rep. Germany) and the IN2P3 (France) for financial support.

APPENDIX A

DEFINITION OF $\omega\pi^0$ DECAY ANGLES

The angles $\Omega = (\cos\theta, \phi)$ describe the direction of the ω in the $\omega\pi$ helicity system.

In the overall γp c.m.s. let $\vec{z}$ be a unit vector along the $\omega\pi^0$ direction, and $\vec{k}$ a unit vector in the beam (γ) direction, then we define

$$\vec{y} = \vec{k} \times \vec{z} / |\vec{k} \times z| \qquad \text{(normal to production plane)}$$

and

$$\vec{x} = \vec{y} \times \vec{z} \ .$$

By a Lorentz transformation along the $\vec{z}$ direction we obtain the momentum vector $(\vec{\omega})$ of the ω in the $\omega\pi^0$ rest frame, then

$$\cos\theta = \vec{\omega} \cdot \vec{z} / |\vec{\omega}|$$

$$\phi = \tan^{-1}\left(\frac{\vec{\omega} \cdot \vec{y}}{\vec{\omega} \cdot \vec{x}}\right) . \qquad \text{(A1)}$$

The angles $\Omega_H = (\cos\theta_H, \phi_H)$ describe the direction of the normal to the $\omega \to 3\pi$ decay plane in the ω helicity system. Let $\vec{z}_H$ be the unit vector in the ω direction in the overall γp c.m.s. Then define

$$\vec{y}_H = \vec{z} \times \vec{z}_H / \left|\vec{z} \times \vec{z}_H\right|$$

$$\vec{x}_H = \vec{y}_H \times \vec{z}_H \ .$$

By a Lorentz transformation along the z_H direction we obtain the momentum vectors $(\vec{\pi}_1, \vec{\pi}_2)$ of the charged πs in the ω rest frame. The normal to the decay plane is then

$$\vec{n} = \vec{\pi}_1 \times \vec{\pi}_2 / |\vec{\pi}_1 \times \vec{\pi}_2| \ ,$$

and

$$\cos\theta_H = \vec{n} \cdot \vec{z}_H$$

$$\phi_H = \tan^{-1}\left(\frac{\vec{n} \cdot \vec{y}_H}{\vec{n} \cdot \vec{z}_H}\right) . \qquad \text{(A2)}$$

The angle Φ defines the polarization vector of the incident photon:

$$\vec{\epsilon} = (\cos \Phi, \sin \Phi, 0), \tag{A3}$$

with respect to the production plane (x-z plane). The spin-density matrix of the plane polarized photon is then [19]

$$\rho(\gamma) = \frac{1}{2}\begin{bmatrix} 1 & -e^{-2i\Phi} \\ -e^{2i\Phi} & 1 \end{bmatrix}. \tag{A4}$$

APPENDIX B

DEFINITION OF ORTHOGONAL MOMENTS

The orthogonal functions $H_\alpha^{\pm}(\Omega,\Omega_H)$ ($\alpha \equiv \ell mLM$) are defined in terms of Wigner D-functions [22]

$$H_\alpha^{\pm}(\Omega,\Omega_H) = \frac{1}{2}\,\mathrm{Re}\left\{D^L_{Mm}(\phi,\theta,0)D^{\ell}_{mo}(\phi_H,\theta_H,0) \pm (-1)^{L+M}D^L_{-Mm}D^{\ell}_{mo}\right\}. \tag{B1}$$

We have listed the explicit expressions for the 25 functions used in this analysis in table 1. Note that these functions are not normalized to unity:

$$C_\alpha = \iint \left[H_\alpha^{\pm}(\Omega,\Omega_H)\right]^2 d\Omega d\Omega_H = (4\pi)^2 / \left\{(2\ell+1)(2L+1)(2-\delta_{mo})(2-\delta_{Mo})\right\}. \tag{B2}$$

APPENDIX C

DEFINITION OF MOMENT SUMS

The moment sums $H_s^{\pm}(\ell mLM)$ are obtained by summing (B1) over all N events:

$$H_s^{\pm}(\alpha) = \frac{1}{N} \sum_{i=1}^{N} H_\alpha^{\pm}(\Omega_i, \Omega_{Hi}) \ . \tag{C1}$$

This sum can be expanded in terms of the contribution from different spin-parity states $(J_i^{\eta_i})$ and their interferences [13],

$$\begin{aligned} H_s^{+}(\alpha) &= \sum_i \text{Re } H_{ii}(\alpha) \\ H_s^{-}(\alpha) &= 2 \sum_{i>j} \text{Re } H_{ij}(\alpha) \end{aligned} \tag{C2}$$

and $$\eta_i \eta_j = -1 \ .$$

The complex sums H_{ij} can then be related to the production density matrix $(\rho^{ij}_{\Lambda\Lambda'})$ and the decay amplitudes (F^i_λ):

$$H_{ij}(\ell mLM) = t^{ij*}_{LM} f^{ij}_{L\ell m} \ \langle 10\ell 0 | 10 \rangle \ , \tag{C3}$$

where

$$t^{ij*}_{LM} = \left(\frac{2J_j+1}{2J_i+1} \right)^{\frac{1}{2}} \sum_{\Lambda\Lambda'} \rho^{ij}_{\Lambda\Lambda'} \ \langle J_j \Lambda' LM | J_i \Lambda \rangle \tag{C4}$$

and

$$f^{ij}_{L\ell m} = \sum_{\lambda\lambda'} F^i_\lambda \ F^{j*}_{\lambda'} \ \langle J_j \lambda' LM | J_i \lambda \rangle \langle 1\lambda' \ell m | 1\lambda \rangle \ . \tag{C5}$$

Parity conservation in the production and decay of the $\omega\pi$ system requires

$$\rho^{ij}_{\Lambda\Lambda'} = \eta_i \eta_j (-1)^{J_i - J_j} (-1)^{\Lambda - \Lambda'} \rho^{ij}_{-\Lambda -\Lambda'} \tag{C6}$$

and

$$F^i_\lambda = \eta_i (-1)^{J_i - 1} F^i_{-\lambda} \ . \tag{C7}$$

Time reversal invariance, for a fixed spin parity state requires

$$F^i_\lambda F^{i*}_{\lambda'} = \text{real} \ . \tag{C8}$$

The decay amplitudes can be expanded in terms of partial wave amplitudes C^i_ℓ:

$$F^i_\lambda = \sum_\ell \left(\frac{2\ell+1}{2J_i+1}\right)^{\frac{1}{2}} \langle J_i \lambda | \ell 0 1 \lambda \rangle C^i_\ell \tag{C9}$$

and

$$\sum_\ell (C^i_\ell)^2 = 1 \ . \tag{C10}$$

A more detailed account of the relations given in this section can be found in the paper of Chung et al. [13]. We list in table 2 the explicit expressions for the 25 moment sums used in this analysis, and note that for the interference moments ($i \neq j$) only the terms Re $\left\{\rho^{ij}_{\Lambda\Lambda'} e^{i\delta_{ij}}\right\}$ appear in the moment sums, where δ_{ij} is the phase difference between the decay amplitudes F^i and F^j.

APPENDIX D

ACCEPTANCE CORRECTIONS

For a plane polarized photon beam, the most general expression for the angular distribution of the $\omega\pi^0$ system is [19]

$$\frac{dN}{d\Omega d\Omega_H d\Phi} = \frac{N}{2\pi}\left[W_0(\Omega,\Omega_H) - PW_1(\Omega,\Omega_H)\cos 2\Phi - PW_2(\Omega,\Omega_H)\sin 2\Phi\right], \tag{D1}$$

where N is the overall normalization, P the mean polarization, and the angles (Ω,Ω_H,Φ) have been defined in section A of this appendix.

Each of the distributions $W_k(\Omega,\Omega_H)(k = 0,1,2)$ can be expanded in terms of the orthogonal moments $H_\alpha(\Omega,\Omega_H)$(Appendix B) [the superscripts +(-) are dropped for clarity; all summations over $\alpha = \ell mLM$ imply summation over +(-) as well]:

$$W_k(\Omega,\Omega_H) = \sum_\alpha H_s^k(\alpha) H_\alpha(\Omega,\Omega_H)/C_\alpha \ , \tag{D2}$$

where

$$\iint H_\alpha(\Omega,\Omega_H) H_\beta(\Omega,\Omega_H) d\Omega d\Omega_H = \delta_{\alpha\beta} C_\alpha \ , \tag{D3}$$

so that

$$H_s^k(\alpha) = \iint W_k(\Omega,\Omega_H) H_\alpha(\Omega,\Omega_H) d\Omega d\Omega_H \ . \tag{D4}$$

Because of the orthogonality of the functions cos 2Φ and sin 2Φ over the interval $0 \le \Phi < 2\pi$, we can define an extended set of orthogonal moments $H_\alpha^k(\Omega,\Omega_H,\Phi)$:

$$\left.\begin{aligned} H_\alpha^0(\Omega,\Omega_H,\Phi) &= H_\alpha(\Omega,\Omega_H) \\ H_\alpha^1(\Omega,\Omega_H,\Phi) &= \sqrt{2}\cos 2\Phi\ H_\alpha(\Omega,\Omega_H) \\ H_\alpha^2(\Omega,\Omega_H,\Phi) &= \sqrt{2}\sin 2\Phi\ H_\alpha(\Omega,\Omega_H) \end{aligned}\right\} \tag{D5}$$

We can also define corresponding moment sums $G_s^k(\alpha)$:

$$NG_s^k(\alpha) = \iiint \frac{dN}{d\Omega d\Omega_H d\Phi} \; H_\alpha^k(\Omega,\Omega_H,\Phi) d\Omega d\Omega_H d\Phi \; , \tag{D6}$$

and using (D1) we obtain

$$\begin{aligned} NG_s^0(\alpha) &= NH_s^0(\alpha) \\ NG_s^1(\alpha) &= -\frac{PN}{\sqrt{2}} \; H_s^1(\alpha) \\ NG_s^2(\alpha) &= -\frac{PN}{\sqrt{2}} \; H_s^2(\alpha) \end{aligned} \tag{D7}$$

Thus, assuming that acceptance corrections have been taken care of, the moment sums $H_s^k(\alpha)$ can be obtained by simply summing the $H_\alpha^k(\Omega,\Omega_H,\Phi)$ over all events ($g_0 = 1$, $g_1 = g_2 = -P/\sqrt{2}$):

$$Ng_k H_s^k(\alpha) = \sum_{i=1}^{N} H_\alpha^k(\Omega_i,\Omega_{H_i},\Phi_i) \; . \tag{D8}$$

In order to understand the effects of acceptance bias, we write the observed angular distribution as

$$\frac{dN'}{d\Lambda'} = \int \frac{dN}{d\Lambda} \in(\Lambda,\Lambda') d\Lambda \; , \tag{D9}$$

where $\Lambda = (\Omega,\Omega_H,\Phi)$ are the true angles and $\Lambda' = (\Omega',\Omega_H',\Phi')$ are the measured angles, and $\in(\Lambda,\Lambda')$ is the acceptance/resolution of the experiment.

Thus, using (D9) and (D6) we obtain the expression for the observed moment sums G'

$$N'G_s'^k(\alpha) = \iint \frac{dN}{d\Lambda} \in(\Lambda,\Lambda') H_\alpha^k(\Lambda') d\Lambda d\Lambda' \; . \tag{D10}$$

We can also expand the true angular distribution in terms of the moments $H_\alpha^k(\Lambda)$:

$$\frac{dN}{d\Lambda} = \sum_{\alpha,k} NG_s^k(\alpha) H_\alpha^k(\Lambda)/2\pi C_\alpha \; , \tag{D11}$$

and substituting this into (D10) we obtain

$$N'G_s'^k(\alpha) = \sum_{j\beta} \frac{NG_s^j(\beta)}{2\pi C_\beta} \iint \epsilon(\Lambda,\Lambda') H_\alpha^k(\Lambda') H_\beta^j(\Lambda) d\Lambda d\Lambda' \tag{D12}$$

or

$$N'G_s'^k(\alpha) = \sum_{j\beta} A_{\alpha\beta}^{kj} NG_s^j(\beta)/C_\beta \ , \tag{D13}$$

where the acceptance/resolution matrix A is given by:

$$A_{\alpha\beta}^{kj} = \frac{1}{2\pi} \iint \epsilon(\Lambda,\Lambda') H_\alpha^k(\Lambda') H_\beta^j(\Lambda) d\Lambda d\Lambda' \ . \tag{D14}$$

If this matrix can be evaluated, (D13) can be inverted to give the corrected moment sums G in terms of the observed moment sums G′:

$$NG_s^j(\beta) = C_\beta \sum_{\alpha k} (A_{\beta\alpha}^{jk})^{-1} N'G_s'^k(\alpha) \ . \tag{D15}$$

In order to evaluate the integral in (D14) we have used a Monte Carlo technique. Events of the type $\gamma p \to \omega\pi^0 p$, with $\omega \to \pi^+\pi^-\pi^0$, were generated isotropically in Λ at fixed values of the $\omega\pi^0$ mass corresponding to the bins used in the analysis. For each event generated, the angles $\Lambda(\Omega,\Omega_H,\Phi)$ were calculated and stored. These events were then passed through the acceptance simulation program, and those surviving were processed using the same analysis as for the data. The integral (D14) was then evaluated as

$$A_{\alpha\beta}^{kj} = \frac{(4\pi)^2}{N_0} \sum_{i=1}^{N} H_\alpha^k(\Lambda_i') H_\beta^j(\Lambda_i) \ , \tag{D16}$$

where N_0 was the number of events generated, N the number accepted, and $\Lambda_i(\Lambda_i')$ the true (reconstructed) angles for event i.

A great simplification of the acceptance matrix can be achieved if the acceptance/resolution of the experiment is unchanged by the transformation $\Phi \to \Phi + \pi/2$ and $\Phi' \to \Phi' + \pi/2$, since in this case the moment sums $G_s^0(\alpha)$ are decoupled from $G_s^k(\alpha)$ where k = 1,2 ($A^{10} = A^{01} = A^{20} = A^{02} = 0$):

$$NG_s^0(\alpha) = C_\alpha \sum_\beta \left(A^{00}_{\alpha\beta}\right)^{-1} N' G_s'^{0}(\beta) \ . \qquad \text{(D17)}$$

This symmetry will be exact if the acceptance is symmetric about the median plane, and we add together two equal samples of data with the same mean polarization, but with the plane of polarization different by $\pi/2$. The first condition is approximately true, and we have ensured the second by reweighting the events according to the measured polarization, keeping the overall normalization fixed. Under these conditions we find, using the Monte Carlo integration (D16),

$$A^{10} = A^{01} = A^{20} = A^{02} = 0$$

and

$$A^{12} = A^{21} = 0 \ ,$$

so that

$$NG_s^j(\alpha) = C_\alpha \sum_\beta \left(A^{jj}_{\alpha\beta}\right)^{-1} N' G_s'^{j}(\beta) \ . \qquad \text{(D18)}$$

We have checked that (D18) does correctly reproduce the moment sums using the acceptance simulation program.

APPENDIX E

MODEL DEPENDENT FIT

In order to investigate the phase relationship between the $J^P = 1^+$ and 1^- states, we have fitted the data simultaneously in all nine mass bins using resonant and non-resonant parametrizations for the decay amplitudes. The parametrization of these amplitudes, the production density matrix, and the resulting moment sums are outlined here.

i) Production density matrix

The unpolarized density matrix was parametrized as

$$\rho^{\alpha\beta}_{\Lambda\Lambda'} = f^{\alpha}_{\Lambda} f^{\beta *}_{\Lambda'} + \eta_\alpha \eta_\beta (-1)^{J_\alpha - J_\beta} (-1)^{\Lambda - \Lambda'} f^{\alpha}_{-\Lambda} f^{\beta *}_{-\Lambda'} , \tag{E1}$$

where η_α is the parity of state α, Λ the helicity, and J_α the spin. For $J = 1$ states, the complex "amplitudes" f^{α}_{Λ} are defined by five real numbers (angles):

$$\begin{aligned} f^{\alpha}_{0} &= \frac{\cos\theta_\alpha}{\sqrt{2}} e^{i\phi^{\alpha}_{0}} && \frac{\pi}{2} \geq \theta_\alpha \geq 0 \\ f^{\alpha}_{+} &= \frac{\sin\theta_\alpha}{\sqrt{2}} \cos\psi_\alpha \, e^{i\phi^{\alpha}_{+}} && 2\pi > \phi^{\alpha}_{\Lambda} \geq 0 \\ f^{\alpha}_{-} &= \frac{\sin\theta_\alpha}{\sqrt{2}} \sin\psi_\alpha \, e^{i\phi^{\alpha}_{-}} && \frac{\pi}{2} \geq \psi_\alpha \geq 0 \end{aligned} \tag{E2}$$

These five angles are assumed to be independent of $M_{\omega\pi^0}$, so that the density matrix elements themselves are also independent of $M_{\omega\pi^0}$, and satisfy (for example):

$$\begin{aligned} \rho^{\alpha\beta}_{\Lambda\Lambda'} &= \eta_\alpha \eta_\beta (-1)^{J_\alpha - J_\beta} (-1)^{\Lambda - \Lambda'} \rho^{\alpha\beta}_{-\Lambda-\Lambda'} \\ \rho^{\alpha\beta}_{\Lambda\Lambda'} &= \rho^{\beta\alpha *}_{\Lambda'\Lambda} \\ \sum_{\Lambda} \rho^{\alpha\alpha}_{\Lambda\Lambda} &= 1 \quad \text{(for each state } \alpha) \\ \left| \rho^{\alpha\beta}_{\Lambda\Lambda'} \right| &\leq \left(\left| \rho^{\alpha\alpha}_{\Lambda\Lambda} \right| \cdot \left| \rho^{\beta\beta}_{\Lambda'\Lambda'} \right| \right)^{\frac{1}{2}} . \end{aligned}$$

Since the density matrix is unchanged by the transformation $\phi_\Lambda^\alpha \to \phi_\Lambda^\alpha + \delta$, we must fix one of these angles, and have chosen ϕ_0^{1+}.

ii) Decay amplitudes

These are parametrized as a function of mass in terms of a resonant Breit-Wigner amplitude $D_\alpha(m)$, a coupling (normalization) constant G_α, and an interaction radius R_α. The decay amplitudes can be expanded using the (real) partial wave amplitudes C_ℓ^α (see C9):

$$F_\lambda^\alpha(m) = D_\alpha(m) G_\alpha \sum_\ell \left(\frac{2\ell+1}{2J_\alpha+1}\right)^{\frac{1}{2}} \langle J_\alpha \lambda | \ell 0 | \lambda \rangle C_\ell^\alpha \frac{B_\ell(m,R_\alpha)}{B_\ell(m_\alpha,R_\alpha)} \ . \tag{E3}$$

The $B_\ell(m,R)$ are barrier penetration factors [23]. Note that for $J^P = 1^-, 0^-$, $C_\ell = 0$ except for $C_1 = 1$, and that for the 1^+ state $D/S = C_2/C_0$. The Breit-Wigner amplitudes are parametrized:

$$D_\alpha(m) = \frac{m_\alpha \Gamma_\alpha}{(m^2 - m_\alpha^2) - i m_\alpha \Gamma_\alpha(m)} \tag{E4}$$

$$\Gamma_\alpha(m) = \Gamma_\alpha\left(\frac{q}{q_\alpha}\right)\left[\frac{B_\ell(m,R_\alpha)}{B_\ell(m_\alpha,R_\alpha)}\right]^2 \ , \tag{E5}$$

where q (q_α) is the ω momentum in the $\omega\pi^0$ c.m.s. with total mass $m(m_\alpha)$. We have checked that the results of fits are not significantly changed by making $\Gamma_\alpha(m)$ independent of mass.

iii) Moment sums

Having defined the production density matrix and decay amplitudes, we can write the moment sum $NH_s^0(\ell m LM)$ averaged over incoming photon energy and integrated over four-momentum transfer t (see Appendix C):

$$N \frac{dH_s^0(\ell m LM)}{dm} = \frac{q\left(e^{Bt_{min}} - e^{Bt_{max}}\right)}{64\pi^3 B} \sum_{\alpha,\beta} \mathrm{Re}\left\{t_{LM}^{\alpha\beta *} f_{L\ell m}^{\alpha\beta}\right\} \ , \tag{E6}$$

where we have assumed that all states α are produced with the same s and t dependence, have taken $B = 5\ \mathrm{GeV}^{-2}$ to agree with the data, and have used the mean photon energy (39 GeV) in calculating the mass dependent factors t_{min} and t_{max}.

The expression (E6) has been used to calculate the expected contribution to each of the 25 moment sums in each of the nine $\omega\pi^0$ mass bins, and thus a χ^2

which was minimized using the program MINUIT [15] to obtain best estimates and errors for the variable parameters (for each state):

M_α	resonant mass
Γ_α	full width of resonance
G_α^2	normalization at resonance
R_α	interaction radius
θ_α, ψ_α, ϕ_Λ^α	five angles which determine the full density matrix
D/S	for the 1^+ state only .

REFERENCES

[1] H.J. Schnitzer, Phys. Rev. 18 (1978) 3482.

[2] A.J. Hey and D. Morgan, Rep. Progr. Phys. 41 (1978) 657.

[3] Particle Data Group, Rev. Particle Properties, Phys. Lett. 111B (1982).

[4] J. Ballam et al., Nucl. Phys. B76 (1974) 375.

[5] D.P. Barber et al., Z. Phys. C4 (1980) 169.
D. Aston et al., Phys. Lett. 92B (1980) 211.

[6] D. Aston et al., Nucl. Instrum. Methods 197 (1982) 287.

[7] P.J. Bussey et al., Nucl. Instrum. Methods 211 (1983) 309.

[8] Experiments at CERN in 1980 (Grey Book) (CERN, Geneva, 1980).

[9] J.C. Lassalle, F. Carena and S. Pensotti, Nucl. Instrum. Methods 176 (1980) 371.

[10] A.P. Waite, MAP Program Guide, University of Manchester (1981), unpublished.

[11] J. Friedman, SAGE Reference Manual, SLAC Computation Group Technical Memo 145 (1972).

[12] M. Atkinson et al., Phys. Lett. 108B (1982) 55.

[13] S.U. Chung et al., Phys. Rev. D11 (1975) 2426.
S.U. Chung, CERN 71-8 (1971).

[14] G. Grayer et al., Nucl. Phys. B75 (1974) 189.

[15] F. James and M. Roos, MINUIT, CERN Computer Centre Program Library Long Write-Up, D506 (1977).

[16] F.M. Renard, Nuovo Cimento 66A (1971) 134.

[17] W.T. Eadie et al., Statistical methods in experimental physics (North Holland Publ. Co., Amsterdam, 1971).

[18] See, for example, ref. 4 and G.W. Brandenburg et al., Nucl. Phys. B16 (1970) 369.

E.L. Berger, A critique of the Reggeized Deck Model, *in* Daresbury Study Weekend No. 8 - DL/R34 (1975).

[19] K. Schilling, P. Seyboth and G. Wolf, Nucl. Phys. B15 (1970) 397.

[20] Atkinson et al., preprint CERN-EP/83-85 (1983), submitted to Nucl. Phys. B.

[21] Atkinson et al., preprint CERN-EP/83-80 (1983), submitted to Nucl. Phys. B.

[22] M.E. Rose, Elementary theory of angular momentum (Wiley & Sons, Inc., New York, 1957).

[23] J.M. Blatt and V.F. Weisskopf, Theoretical nuclear physics (Wiley & Sons, Inc., New York, 1952).

Table 1

$H^{\pm}_{\ell mLM}(\cos\theta, \phi, \cos\theta_H, \phi_H)$

1	$H^+(0000)$	1
2	$H^+(0020)$	$\frac{1}{2}(3\cos^2\theta-1)$
3	$H^+(0021)$	$-\sqrt{\frac{3}{2}}\sin\theta\cos\theta\cos\phi$
4	$H^+(0022)$	$\sqrt{\frac{6}{4}}\sin^2\theta\cos(2\phi)$
5	$H^+(2000)$	$\frac{1}{2}(3\cos^2\theta_H-1)$
6	$H^+(2020)$	$\frac{1}{4}(3\cos^2\theta_H-1)(3\cos^2\theta-1)$
7	$H^+(2021)$	$-\frac{1}{2}\sqrt{\frac{3}{2}}\sin\theta\cos\theta\cos\phi\,(3\cos^2\theta_H-1)$
8	$H^+(2022)$	$\sqrt{\frac{6}{8}}\sin^2\theta\cos(2\phi)\,(3\cos^2\theta_H-1)$
9	$H^+(2120)$	$-\frac{3}{2}\sin\theta\cos\theta\sin\theta_H\cos\theta_H\cos\phi_H$
10	$H^+(2121)$	$-\frac{1}{4}\sqrt{\frac{3}{2}}\sin\theta_H\cos\theta_H\left\{(1+\cos\theta)(2\cos\theta-1)\cos(\phi+\phi_H)-(1-\cos\theta)(2\cos\theta+1)\cos(\phi_H-\phi)\right\}$
11	$H^+(2122)$	$\frac{1}{4}\sqrt{\frac{3}{2}}\sin\theta\sin\theta_H\cos\theta_H\left\{(1+\cos\theta)\cos(2\phi+\phi_H)-(1-\cos\theta)\cos(2\phi-\phi_H)\right\}$
12	$H^+(2220)$	$\frac{3}{8}\sin^2\theta\sin^2\theta_H\cos(2\phi_H)$
13	$H^+(2221)$	$\frac{1}{4}\sqrt{\frac{3}{8}}\sin\theta\sin^2\theta_H\left\{(1+\cos\theta)\cos(2\phi_H+\phi)-(1-\cos\theta)\cos(2\phi_H-\phi)\right\}$
14	$H^+(2222)$	$\frac{1}{8}\sqrt{\frac{3}{8}}\sin^2\theta_H\left\{(1+\cos\theta)^2\cos(2\phi+2\phi_H)+(1-\cos\theta)^2\cos(2\phi-2\phi_H)\right\}$
15	$H^+(2111)$	$-\frac{1}{4}\sqrt{\frac{3}{2}}\sin\theta_H\cos\theta_H\left\{(1+\cos\theta)\cos(\phi+\phi_H)+(1-\cos\theta)\cos(\phi-\phi_H)\right\}$
16	$H^-(0010)$	$\cos\theta$
17	$H^-(0011)$	$-\sqrt{\frac{1}{2}}\sin\theta\cos\phi$
18	$H^-(2110)$	$-\frac{\sqrt{3}}{2}\sin\theta\sin\theta_H\cos\theta_H\cos\phi_H$
19	$H^-(2111)$	$\frac{1}{4}\sqrt{\frac{3}{2}}\sin\theta_H\cos\theta_H\left\{(1-\cos\theta)\cos(\phi-\phi_H)-(1+\cos\theta)\cos(\phi+\phi_H)\right\}$
20	$H^-(2121)$	$-\frac{1}{4}\sqrt{\frac{3}{2}}\sin\theta_H\cos\theta_H\left\{(1+\cos\theta)(2\cos\theta-1)\cos(\phi+\phi_H)+(1-\cos\theta)(2\cos\theta+1)\cos(\phi-\phi_H)\right\}$
21	$H^-(2122)$	$\frac{1}{4}\sqrt{\frac{3}{2}}\sin\theta\sin\theta_H\cos\theta_H\left\{(1+\cos\theta)\cos(2\phi+\phi_H)+(1-\cos\theta)\cos(2\phi-\phi_H)\right\}$
22	$H^-(2221)$	$\frac{1}{4}\sqrt{\frac{3}{8}}\sin\theta\sin^2\theta_H\left\{(1+\cos\theta)\cos(2\phi_H+\phi)+(1-\cos\theta)\cos(2\phi_H-\phi)\right\}$
23	$H^-(2222)$	$\frac{1}{8}\sqrt{\frac{3}{8}}\sin^2\theta_H\left\{(1+\cos\theta)^2\cos(2\phi+2\phi_H)-(1-\cos\theta)^2\cos(2\phi-2\phi_H)\right\}$
24	$H^-(2010)$	$\frac{1}{2}\cos\theta\,(3\cos^2\theta_H-1)$
25	$H^-(2011)$	$-\frac{1}{2\sqrt{2}}\sin\theta\cos\phi\,(3\cos^2\theta_H-1)$

Table 2

Unpolarized moment sums $NH_S^0(\ell mLM)$

1	$NH_S^+(0000)$	$N^+ + N^- + N^0$
2	$NH_S^+(0020)$	$\frac{1}{5} N^+(3\rho_{00}^+-1)(1-3F_1^2) - \frac{1}{10} N^-(3\rho_{00}^--1)$
3	$NH_S^+(0021)$	$\frac{2\sqrt{3}}{5} N^+\rho_{10}^+(1-3F_1^2) - \frac{\sqrt{3}}{5} N^-\rho_{10}^-$
4	$NH_S^+(0022)$	$-\frac{\sqrt{6}}{5} \rho_{1-1}^+(1-3F_1^2) + \frac{\sqrt{6}}{10} N^-\rho_{1-1}^-$
5	$NH_S^+(2000)$	$\frac{2}{5} N^+(1-3F_1^2) - \frac{N^-}{5} + \frac{2}{5} N^0$
6	$NH_S^+(2020)$	$\frac{N^+}{25} (3\rho_{00}^+-1)(2-3F_1^2) + \frac{N^-}{50} (3\rho_{00}^--1)$
7	$NH_S^+(2021)$	$\frac{2\sqrt{3}}{25} N^+\rho_{10}^+(2-3F_1^2) + \frac{\sqrt{3}}{25} N^-\rho_{10}^-$
8	$NH_S^+(2022)$	$\frac{-\sqrt{6}}{25} N^+\rho_{1-1}^+(2-3F_1^2) - \frac{\sqrt{6}}{50} N^-\rho_{1-1}^-$
9	$NH_S^+(2120)$	$\frac{3N^+}{25} (3\rho_{00}^+-1)F_1F_0$
10	$NH_S^+(2121)$	$\frac{6\sqrt{3}}{25} N^+\rho_{10}^+F_1F_0$
11	$NH_S^+(2122)$	$\frac{-3\sqrt{6}}{25} N^+\rho_{1-1}^+F_1F_0$
12	$NH_S^+(2220)$	$\frac{3}{25} N^+(3\rho_{00}^+-1)F_1^2 - \frac{3N^-}{50} (3\rho_{00}^--1)$
13	$NH_S^+(2221)$	$\frac{6\sqrt{3}}{25} N^+\rho_{10}^+F_1^2 - \frac{3\sqrt{3}}{25} N^-\rho_{10}^-$
14	$NH_S^+(2222)$	$\frac{-3\sqrt{6}}{25} N^+\rho_{1-1}^+F_1^2 + \frac{3\sqrt{6}}{50} N^-\rho_{1-1}^-$
15	$NH_S^+(2111)$	$\frac{\sqrt{2}}{5} (N^0N^-)^{\frac{1}{2}} \rho_{01}^{0-}$
16	$NH_S^-(0010)$	$2\sqrt{2} (N^+N^-)^{\frac{1}{2}} \rho_{11}^{+-}F_1 + \frac{2}{\sqrt{3}} (N^0N^+)^{\frac{1}{2}} \rho_{00}^{0+} F_0$
17	$NH_S^-(0011)$	$-\sqrt{2} (N^+N^-)^{\frac{1}{2}} (\rho_{01}^{+-} + \rho_{10}^{+-})F_1 + \frac{2}{\sqrt{3}} (N^0N^+)^{\frac{1}{2}} \rho_{01}^{0+}F_0$
18	$NH_S^-(2110)$	$\frac{-\sqrt{6}}{5} (N^+N^-)^{\frac{1}{2}} \rho_{11}^{+-}F_0 + \frac{2}{5} (N^0N^+)^{\frac{1}{2}} \rho_{00}^{0+}F_1$
19	$NH_S^-(2111)$	$\frac{1}{5}\sqrt{\frac{3}{2}} (N^+N^-)^{\frac{1}{2}} (\rho_{01}^{+-} + \rho_{10}^{+-})F_0 + \frac{2}{5} (N^0N^+)^{\frac{1}{2}} \rho_{01}^{0+}F_1$
20	$NH_S^-(2121)$	$\frac{3}{25}\sqrt{\frac{3}{2}} (N^+N^-)^{\frac{1}{2}} (\rho_{01}^{+-} - \rho_{10}^{+-})F_0$
21	$NH_S^-(2122)$	$\frac{3\sqrt{3}}{25} (N^+N^-)^{\frac{1}{2}} \rho_{1-1}^{+-}F_0$
22	$NH_S^-(2221)$	$\frac{6}{25}\sqrt{\frac{3}{2}} (N^+N^-)^{\frac{1}{2}}(\rho_{01}^{+-} - \rho_{10}^{+-})F_1$
23	$NH_S^-(2222)$	$\frac{6\sqrt{3}}{25} (N^+N^-)^{\frac{1}{2}} \rho_{1-1}^{+-}F_1$
24	$NH_S^-(2010)$	$\frac{-2\sqrt{2}}{5}(N^+N^-)^{\frac{1}{2}} \rho_{11}^{+-}F_1 + \frac{4}{5\sqrt{3}} (N^0N^+)^{\frac{1}{2}} \rho_{00}^{0+}F_0$
25	$NH_S^-(2011)$	$\frac{\sqrt{2}}{5} (N^+N^-)^{\frac{1}{2}} (\rho_{01}^{+-} + \rho_{10}^{+-})F_1 + \frac{4}{5\sqrt{3}} (N^0N^+)^{\frac{1}{2}} \rho_{01}^{0+}F_0$

Table 3

Results of model dependent fit with a resonant 1^+ state and a 1^- state parametrized as the $\rho^0(770)$ tail (fig. 9)

Degrees of freedom	208
χ^2	298
$M(1^+)$ (GeV)	1.213 ± 0.005
$\Gamma(1^+)$ (GeV)	0.231 ± 0.014
D/S	0.235 ± 0.047
$\rho_{00}(1^+)$	0.434 ± 0.031
$\rho_{1-1}(1^+)$	0.095 ± 0.088
Re $\rho_{10}(1^+)$	-0.090 ± 0.070
$M(1^-)$	0.770 (fixed)
$\Gamma(1^-)$	0.401 ± 0.100
$\rho_{00}(1^-)$	0.031 ± 0.060
$\rho_{1-1}(1^-)$	0.00 ± 0.145
Re $\rho_{10}(1^-)$	-0.083 ± 0.068
Re $\rho_{11}(1^+/1^-$ int.)	0.085 ± 0.145
Im $\rho_{11}(1^+/1^-$ int.)	0.333 ± 0.076
Re $\rho_{1-1}(1^+/1^-$ int.)	0.100 ± 0.055
Im $\rho_{1-1}(1^+/1^-$ int.)	-0.094 ± 0.076
Re $\rho_{10}(1^+/1^-$ int.)	0.026 ± 0.067
Im $\rho_{10}(1^+/1^-$ int.)	-0.072 ± 0.060
Re $\rho_{01}(1^+/1^-$ int.)	0.141 ± 0.100
Im $\rho_{01}(1^+/1^-$ int.)	-0.292 ± 0.065

The quoted errors are from MINUIT

Table 4

Results of Model Dependent fits
which are insensitive to the model assumptions.
The quoted statistical errors are from MINUIT,
and the systematic errors indicate the spread in results
for the different model assumptions described in the text.

Parameter	Value	Stat.	Syst.
$M(1^+)$ (GeV)	1.217	± 0.005	± 0.005
$\Gamma(1^+)$ (GeV)	0.231	± 0.014	± 0.020
D/S	0.236	± 0.047	± 0.009
$\rho_{00}(1^+)$	0.435	± 0.030	± 0.006
Re $\rho_{10}(1^+)$	-0.082	± 0.070	± 0.012
$\rho_{1-1}(1^+)$	0.088	± 0.090	± 0.012
$\rho_{00}(1^-)$	0.029	± 0.060	± 0.021
Re $\rho_{10}(1^-)$	-0.065	± 0.070	± 0.035
$\rho_{1-1}(1^-)$	0.029	± 0.150	± 0.060

Figure captions

Fig. 1 : a) Incident photon energy spectrum. b) Incident photon polarization spectrum.

Fig. 2 : Experimental layout and Omega spectrometer.

Fig. 3 : a) Missing mass squared (M_X^2); $\gamma p \to \pi^+\pi^-\pi^0\pi^0 X$. b) Missing mass squared (M_X^2); $\gamma p \to \omega\pi^0 X$.

Fig. 4 : $\gamma p \to \pi^+\pi^-\pi^0\pi^0 p$; $m_{\pi^+\pi^-\pi^0}$ (two entries per event).

Fig. 5 : $\gamma p \to \pi^+\pi^-\pi^0\pi^0 p$; the 1^- decay matrix element squared: $\lambda = 4|\vec{p}_{\pi^+} \times \vec{p}_{\pi^-}|^2 / 3\left[\frac{1}{9}\, m_{3\pi}^2 - m_{\pi^-}^2\right]^2$ in the ω peak (Fig. 5a) and wings (Fig. 5b).

Fig. 6 : $\gamma p \to \pi^+\pi^-\pi^0\pi^0 p$; $m_{\pi^+\pi^-\pi^0\pi^0}$

$\gamma p \to \omega\pi^0 p$; $m_{\omega\pi^0}$ (shaded).

Fig. 7 : $\gamma p \to \omega\pi^0 p$; t, the four-momentum transfer squared between γ and $\omega\pi^0$.

Fig. 8 : $\gamma p \to \omega\pi^0 p$; cos θ, ϕ, cos θ_H and ϕ_H distributions (not corrected for acceptance). The smooth curves are the result of a simulation described in the text.

Fig. 9 : $\gamma p \to \omega\pi^0 p$; acceptance corrected moment sums $NH_s^{\pm}(\ell m L M)$ as a function of $m_{\omega\pi^0}$. The dashed curves are from the model dependent fit described in the text.

Fig. 10 : Model independent fit with $J^P = 0^-, 1^+, 1^-$ to the acceptance corrected moment sums (Fit 1):

a) $J^P = 1^+$ intensity.

b) $J^P = 1^-$ intensity.

c) $J^P = 0^-$ intensity.

d) $J^P = 1^+$ D/S ratio.

e) $J^P = 1^+$ ρ^0_{00}.

f) $J^P = 1^-$ ρ^0_{00}.

Fig. 11 : Model independent fit with $J^P = 1^+$ and 1^- to the acceptance corrected moment sums (Fit 2):

a) $J^P = 1^+$ intensity.

b) $J^P = 1^-$ intensity.

c) $J^P = 1^+$ D/S ratio.

d) $J^P = 1^+$ ρ^0_{00}.

e) $J^P = 1^-$ ρ^0_{00}.

Fig. 12 : Model independent fit with $J^P = 1^+$ and 1^- to the acceptance corrected moment sums, with the 1^- state constrained to be SCHC:

a) $J^P = 1^+$ intensity.

b) $J^P = 1^-$ intensity.

c) $J^P = 1^+$ D/S ratio.

d) $J^P = 1^+$ ρ^0_{00}.

e) $J^P = 1^+$ ρ^0_{+1-1}.

f) $J^P = 1^+$ Re ρ^0_{+10}.

g) $J^P = 1^+/1^-$ interference ρ^0_{11}.

h) $J^P = 1^+/1^-$ interference ρ^0_{01}.

i) $J^P = 1^+/1^-$ interference ρ^0_{1-1}.

Fig. 13 : Energy dependence of $\sigma(\gamma p \to \omega\pi^0 p)$. The dashed curves represent the ±1 standard deviation limits from a fit to the data of this experiment to the form (in the energy range $20 \leq E_\gamma \leq 70$ GeV):

$$\sigma(E_\gamma) = \sigma(39)\left(\frac{39}{E_\gamma}\right)^\alpha \left(e^{Bt_{min}} - e^{Bt_{max}}\right),$$

where $B = 5\ \text{GeV}^{-2}$ and $m_{\omega\pi^0} = 1.25$ GeV were fixed to give an appropriate form for the threshold dependence.

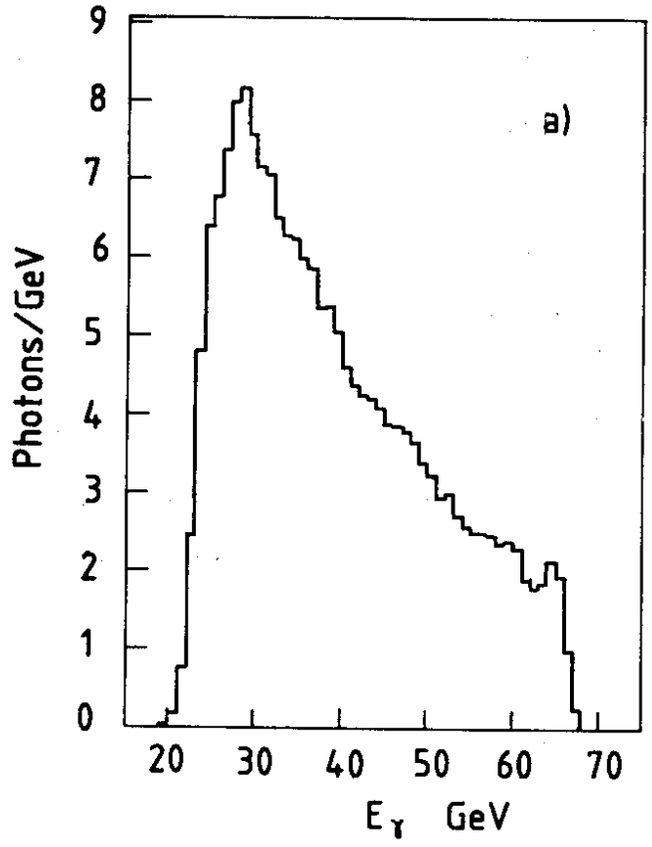
a)
Photons/GeV
9
8
7
6
5
4
3
2
1
0
20
30
40
50
60
70
E_γ GeV

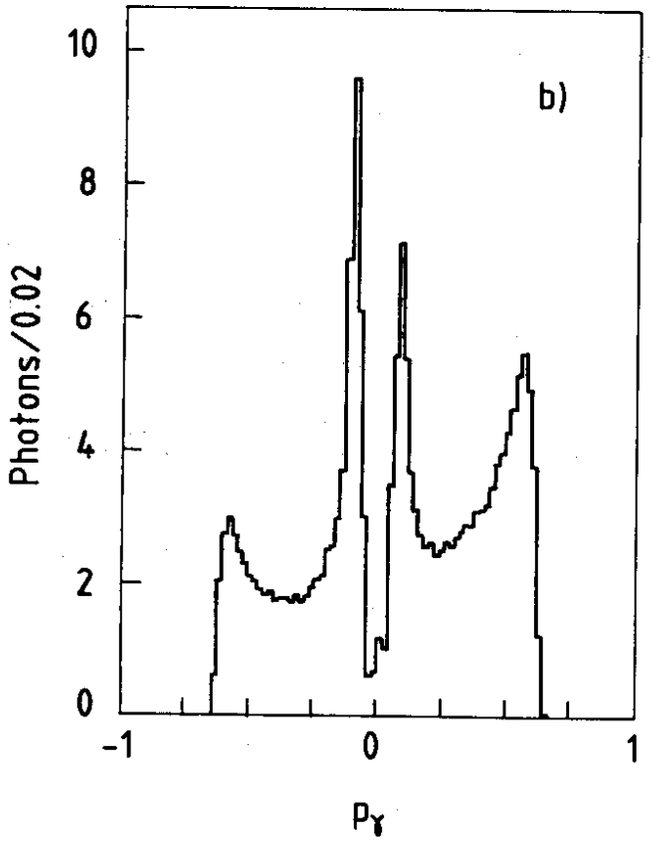
b)
Photons/0.02
10
8
6
4
2
0
-1
0
1
P_γ

Fig. 1

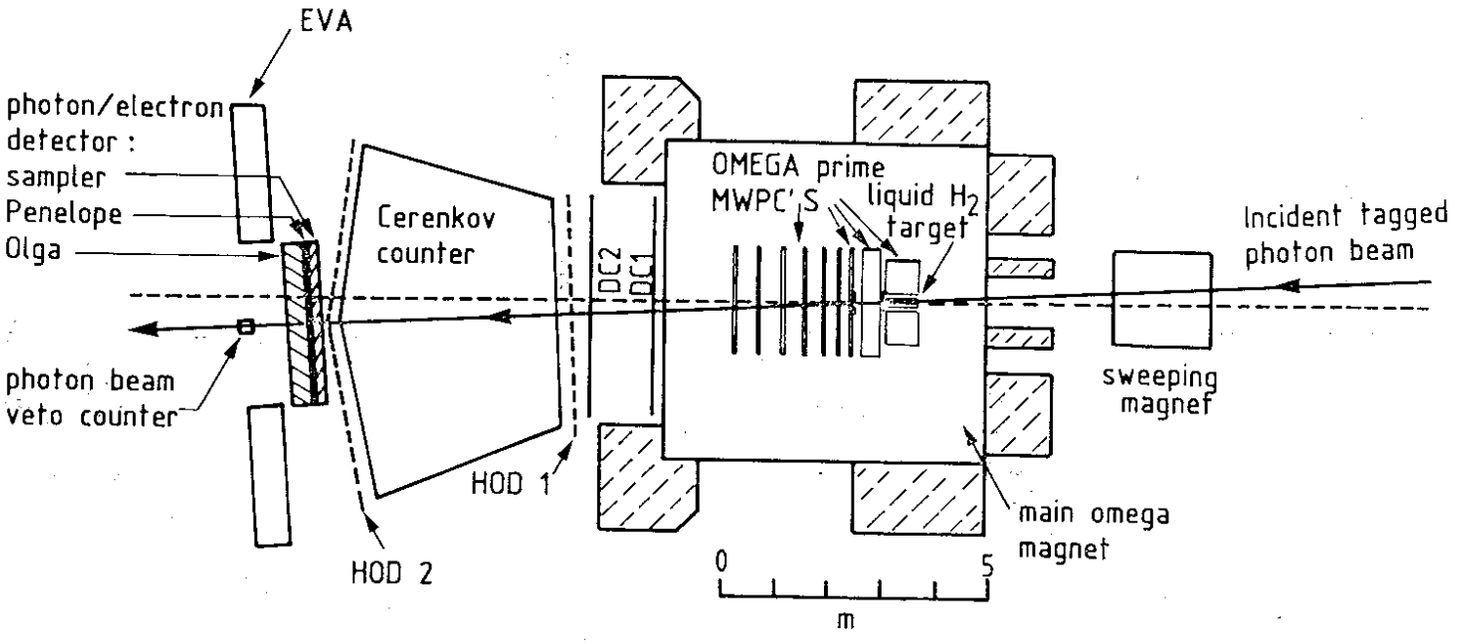
EVA
photon/electron
detector :
sampler
Penelope
Olga
photon beam
veto counter
Cerenkov
counter
DC2
DC1
HOD 1
HOD 2
OMEGA prime
MWPC'S
liquid H_2
target
Incident tagged
photon beam
sweeping
magnef
main omega
magnet
0
5
m

Fig. 2

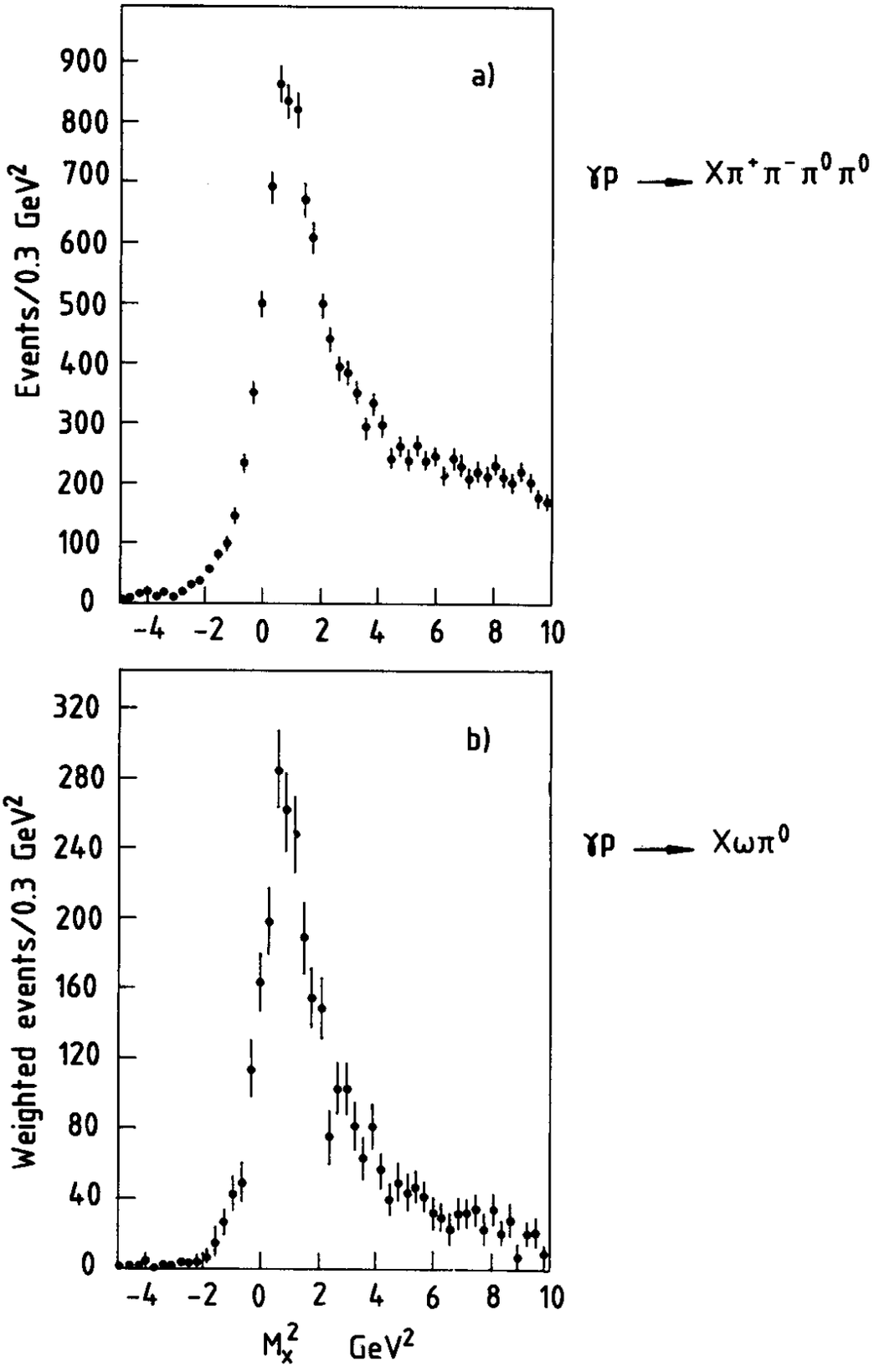
a)
Events/0.3 GeV²
900
800
700
600
500
400
300
200
100
0
-4
-2
0
2
4
6
8
10
γp → Xπ⁺π⁻π⁰π⁰
b)
Weighted events/0.3 GeV²
320
280
240
200
160
120
80
40
0
M²x GeV²
γp → Xωπ⁰

Fig. 3

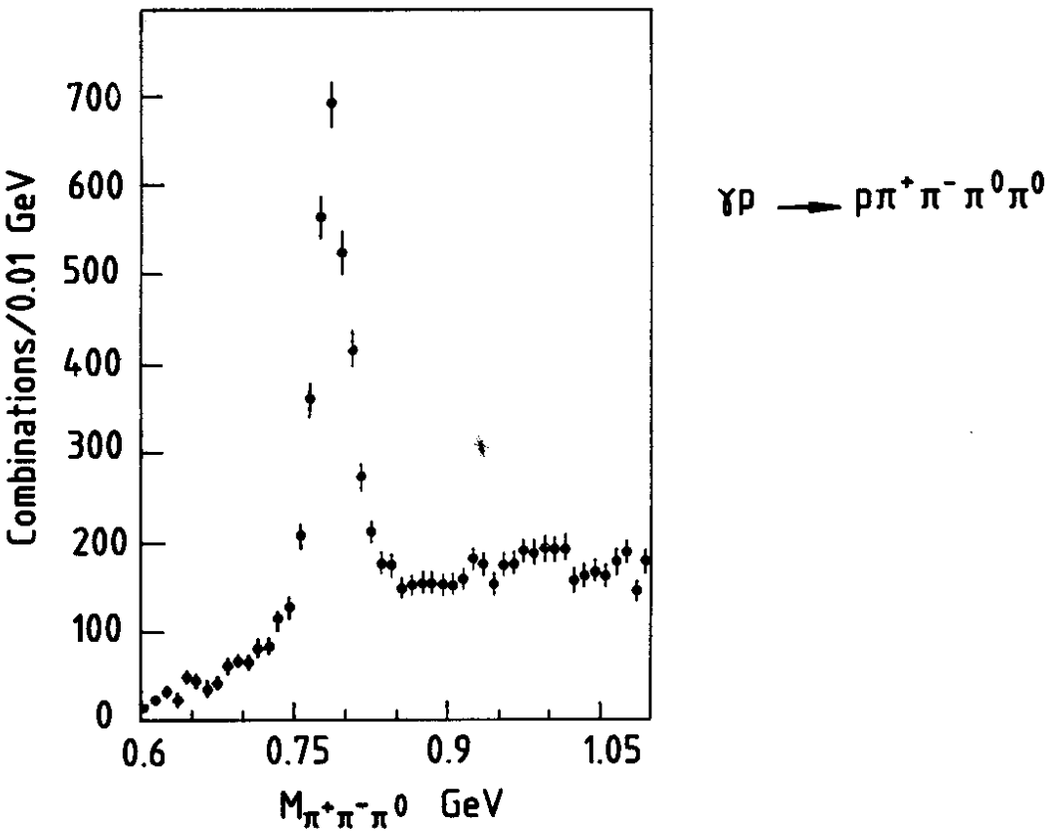
Combinations/0.01 GeV
700
600
500
400
300
200
100
0
0.6
0.75
0.9
1.05
$M_{\pi^+\pi^-\pi^0}$ GeV
$\gamma p \rightarrow p\pi^+\pi^-\pi^0\pi^0$

Fig. 4

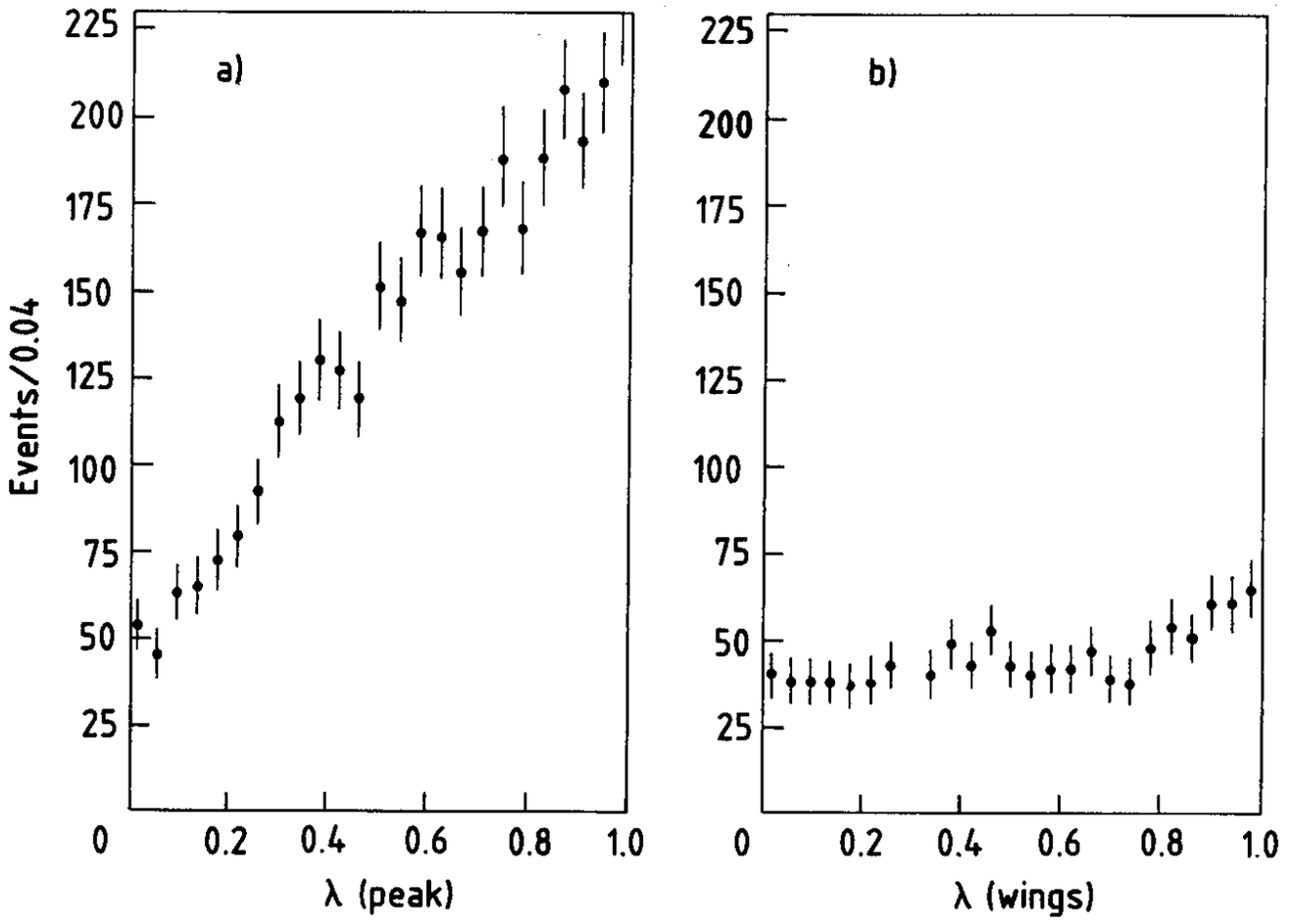
Events/0.04
225
200
175
150
125
100
75
50
25
0
0.2
0.4
0.6
0.8
1.0
a)
λ (peak)
b)
λ (wings)

Fig. 5

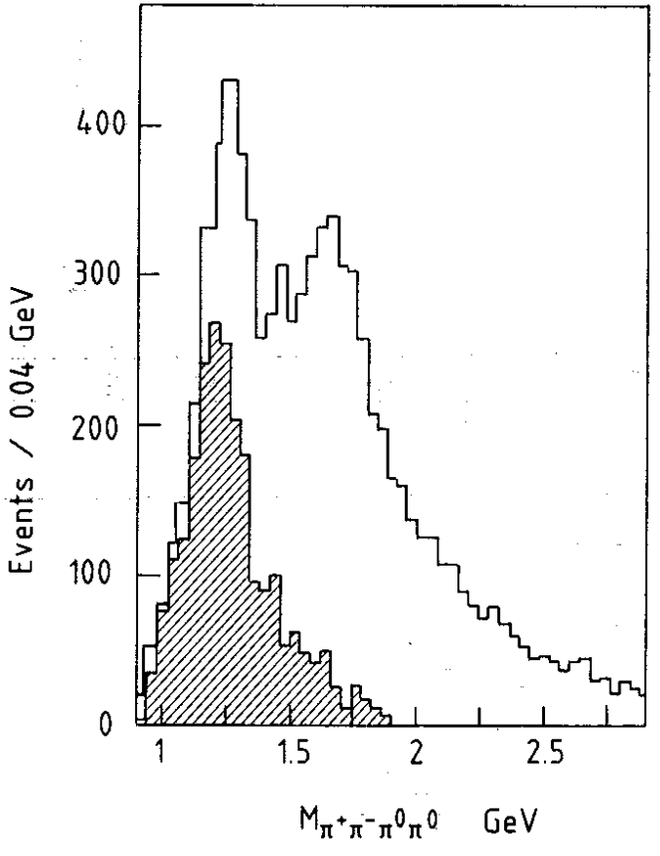
Events / 0.04 GeV
400
300
200
100
0
1
1.5
2
2.5
$M_{\pi^+\pi^-\pi^0\pi^0}$ GeV

Fig. 6

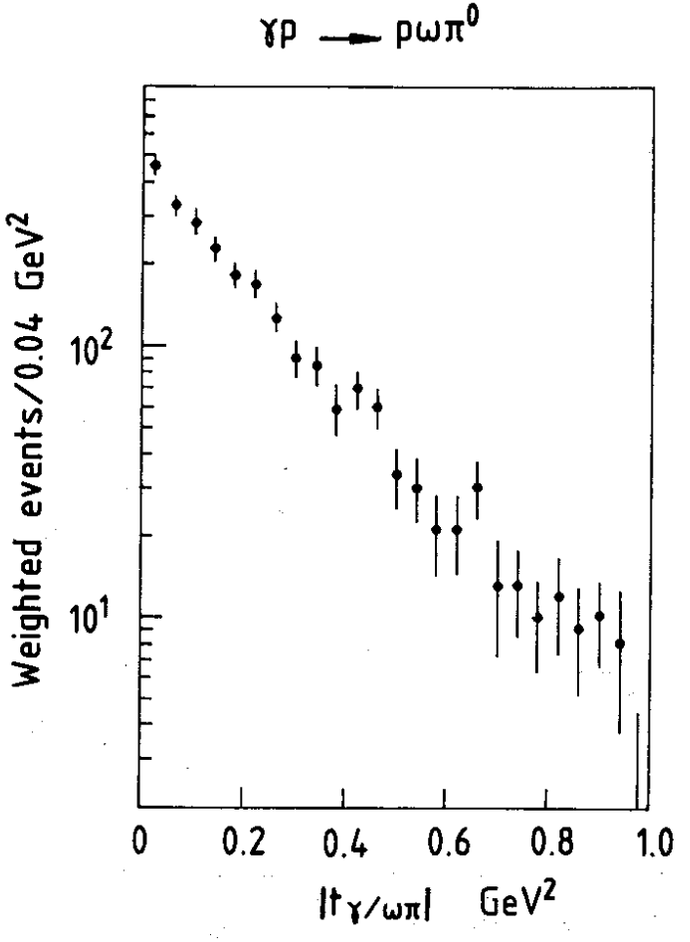
$\gamma p \rightarrow p\omega\pi^0$
Weighted events/0.04 GeV^2
10^2
10^1
0
0.2
0.4
0.6
0.8
1.0
$|t_{\gamma/\omega\pi}|$ GeV^2

Fig. 7

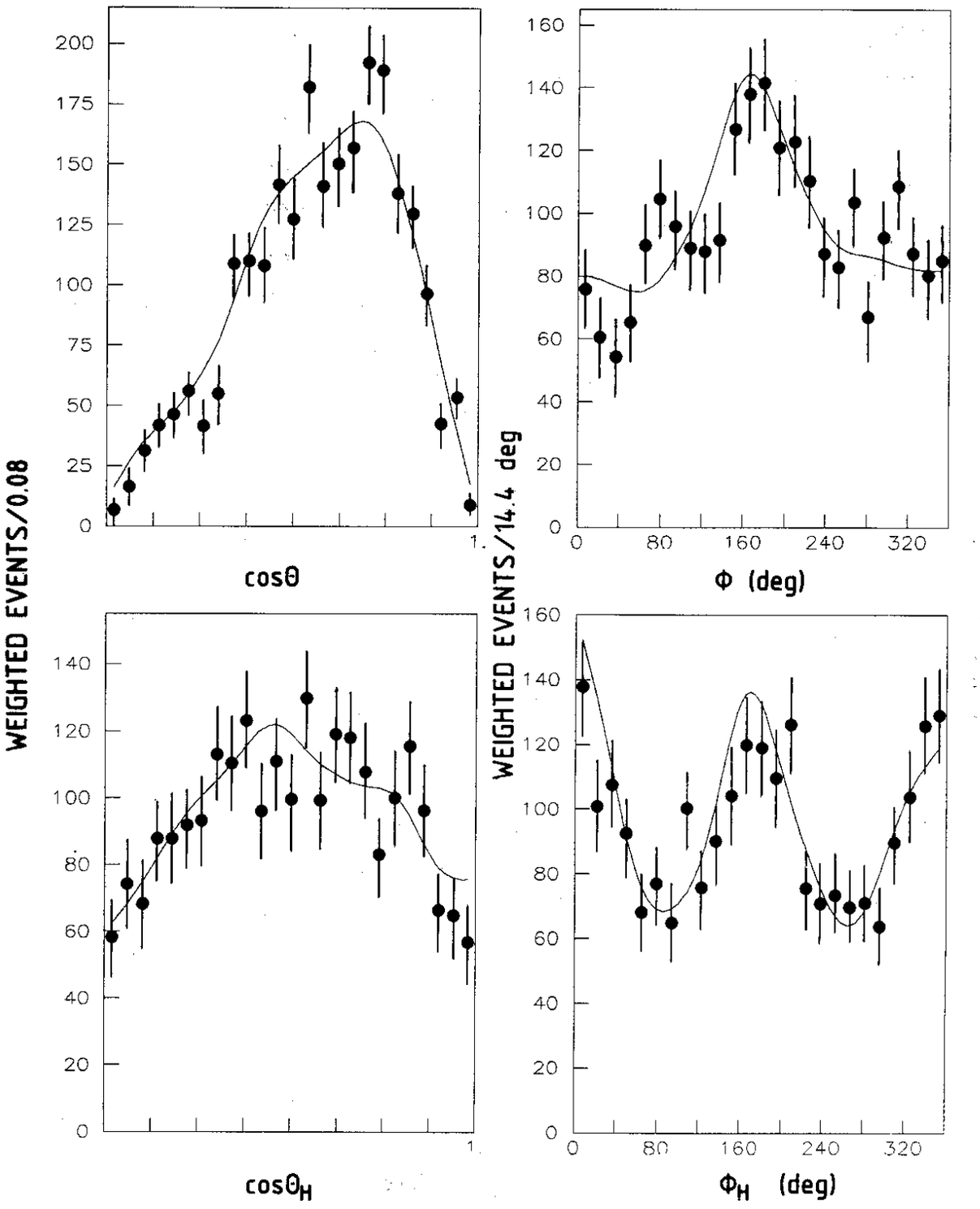
WEIGHTED EVENTS/0.08
cosθ
WEIGHTED EVENTS/14.4 deg
Φ (deg)
cosθH
ΦH (deg)

Fig. 8

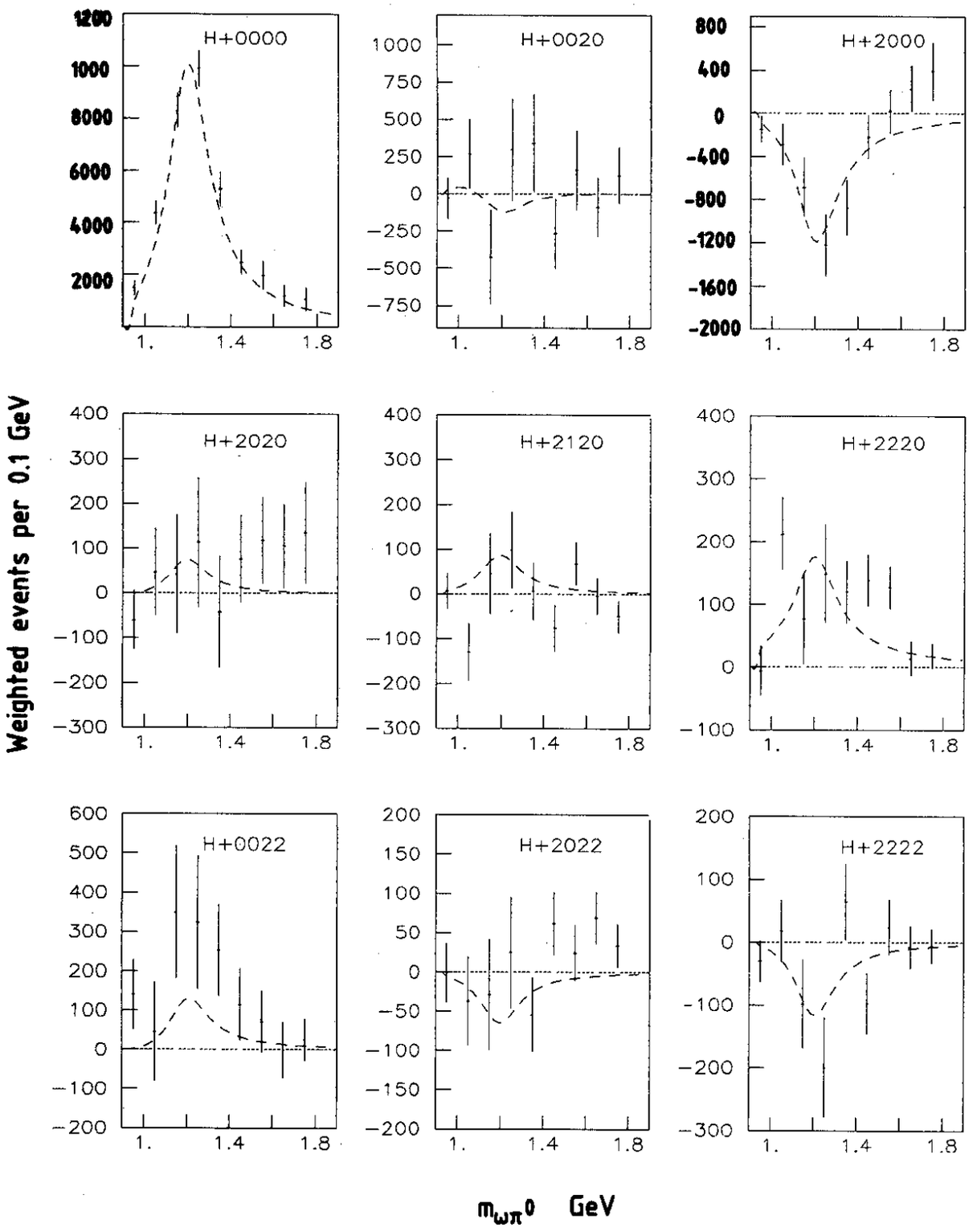
H+0000
H+0020
H+2000
H+2020
H+2120
H+2220
H+0022
H+2022
H+2222
Weighted events per 0.1 GeV
$m_{\omega\pi^0}$ GeV

Fig. 9a

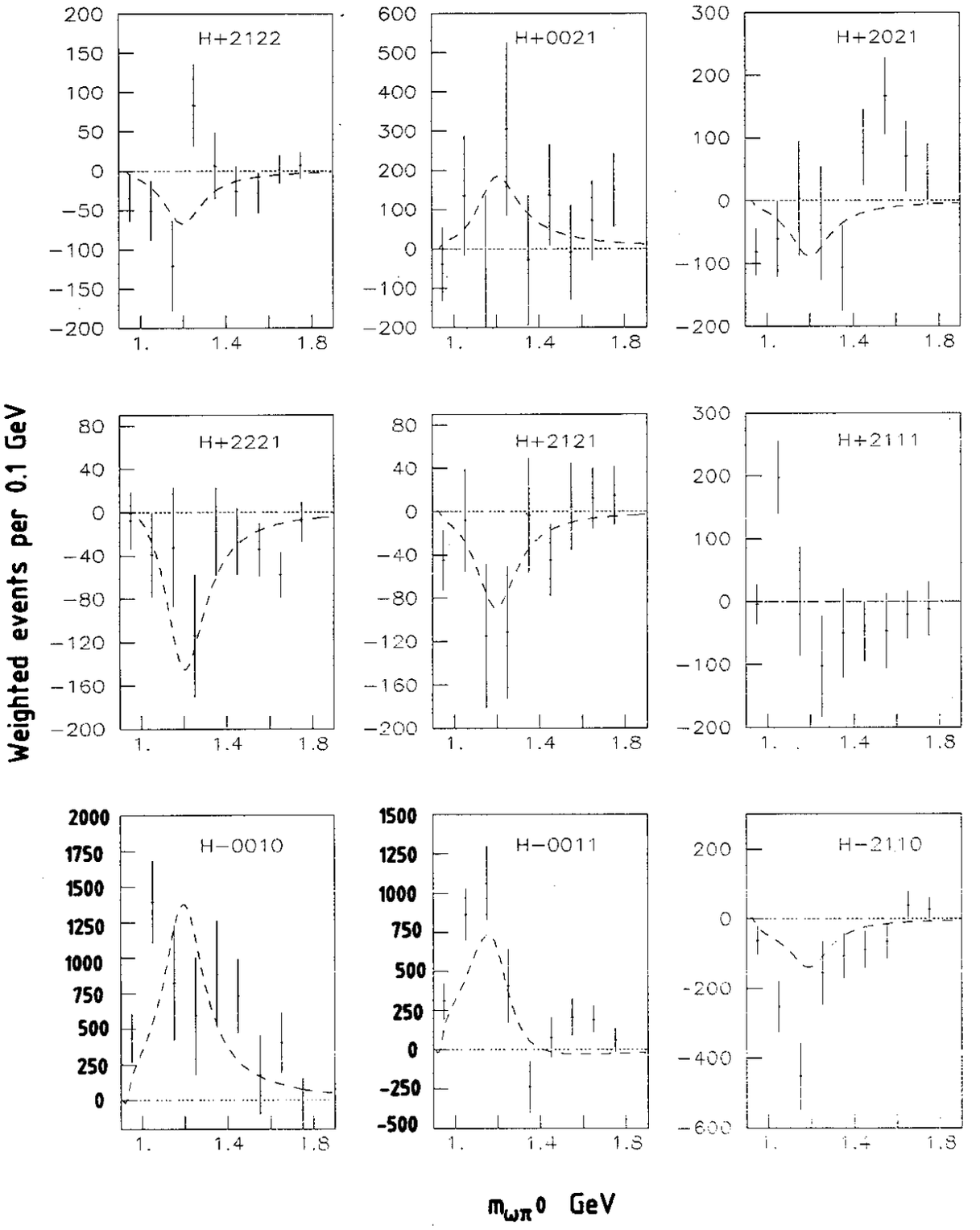
H+2122
H+0021
H+2021
H+2221
H+2121
H+2111
H−0010
H−0011
H−2110
Weighted events per 0.1 GeV
$m_{\omega\pi^0}$ GeV

Fig. 9b

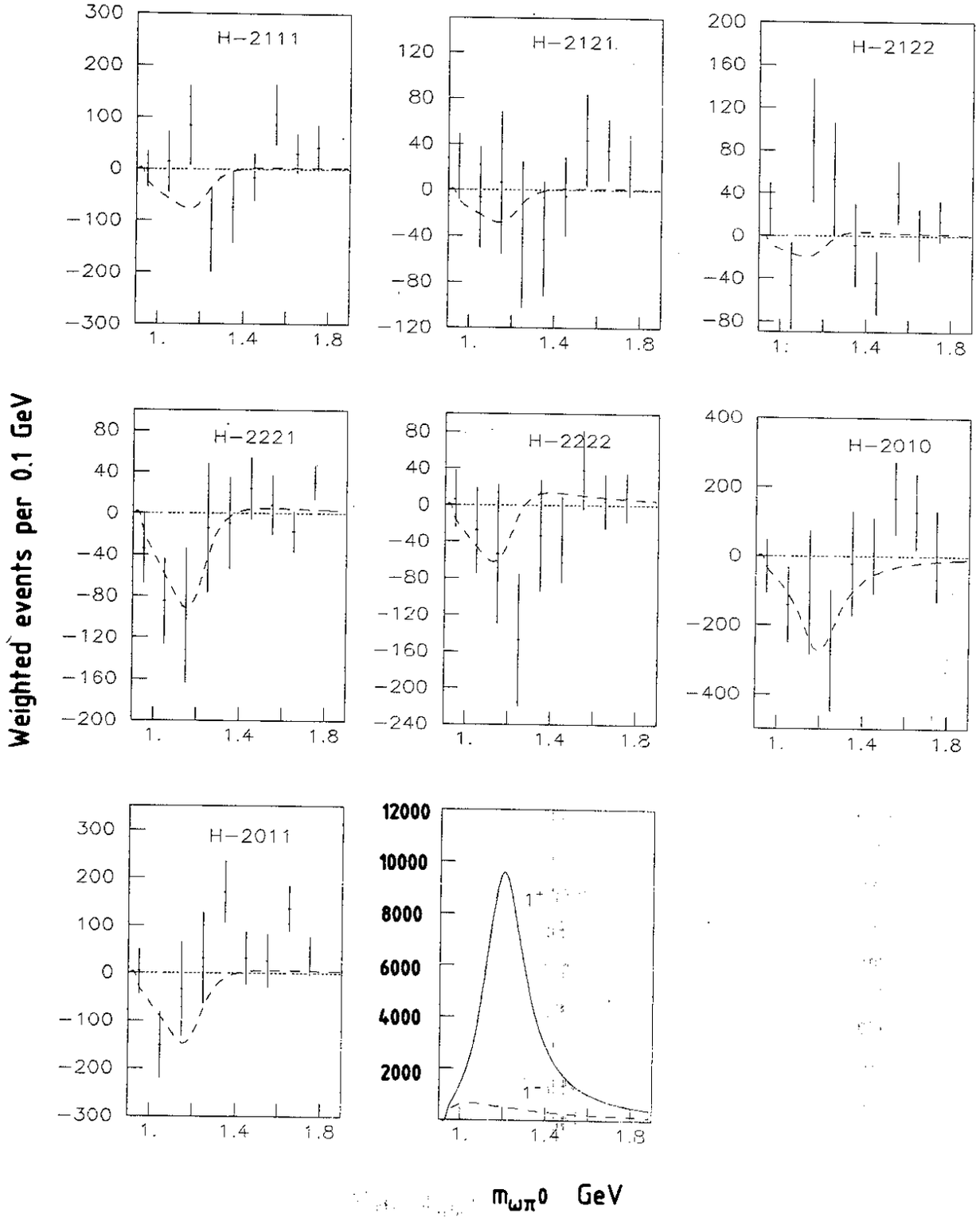
H−2111
H−2121
H−2122
H−2221
H−2222
H−2010
H−2011
1+
1−
Weighted events per 0.1 GeV
$m_{\omega\pi^0}$ GeV

Fig. 9c

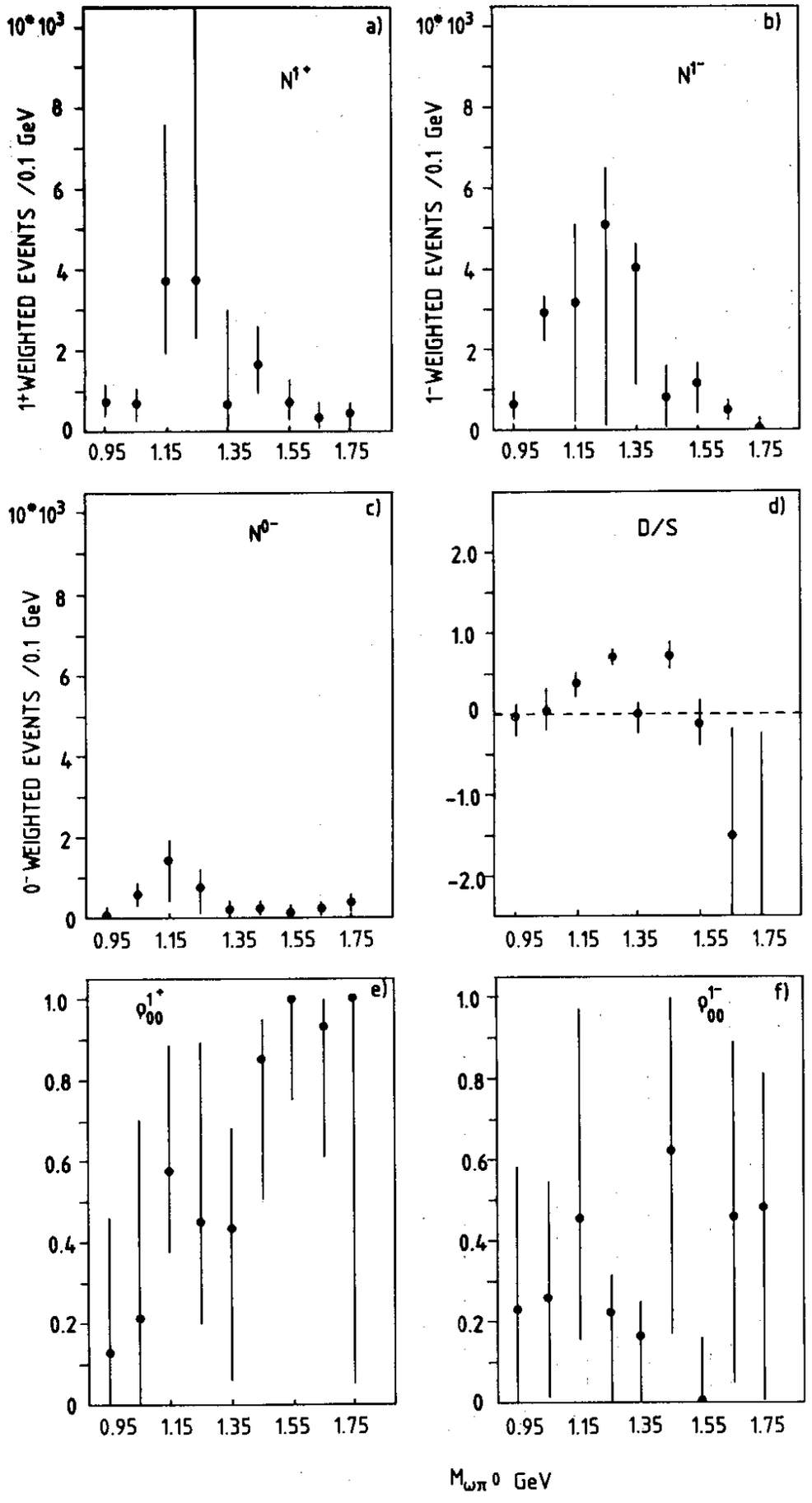
a)
N^{1^+}
$10^* 10^3$
1^+ WEIGHTED EVENTS /0.1 GeV
b)
N^{1^-}
1^- WEIGHTED EVENTS /0.1 GeV
c)
N^{0^-}
0^- WEIGHTED EVENTS /0.1 GeV
d)
D/S
e)
$\rho_{00}^{1^+}$
f)
$\rho_{00}^{1^-}$
0.95 1.15 1.35 1.55 1.75
$M_{\omega\pi^0}$ GeV

Fig. 10

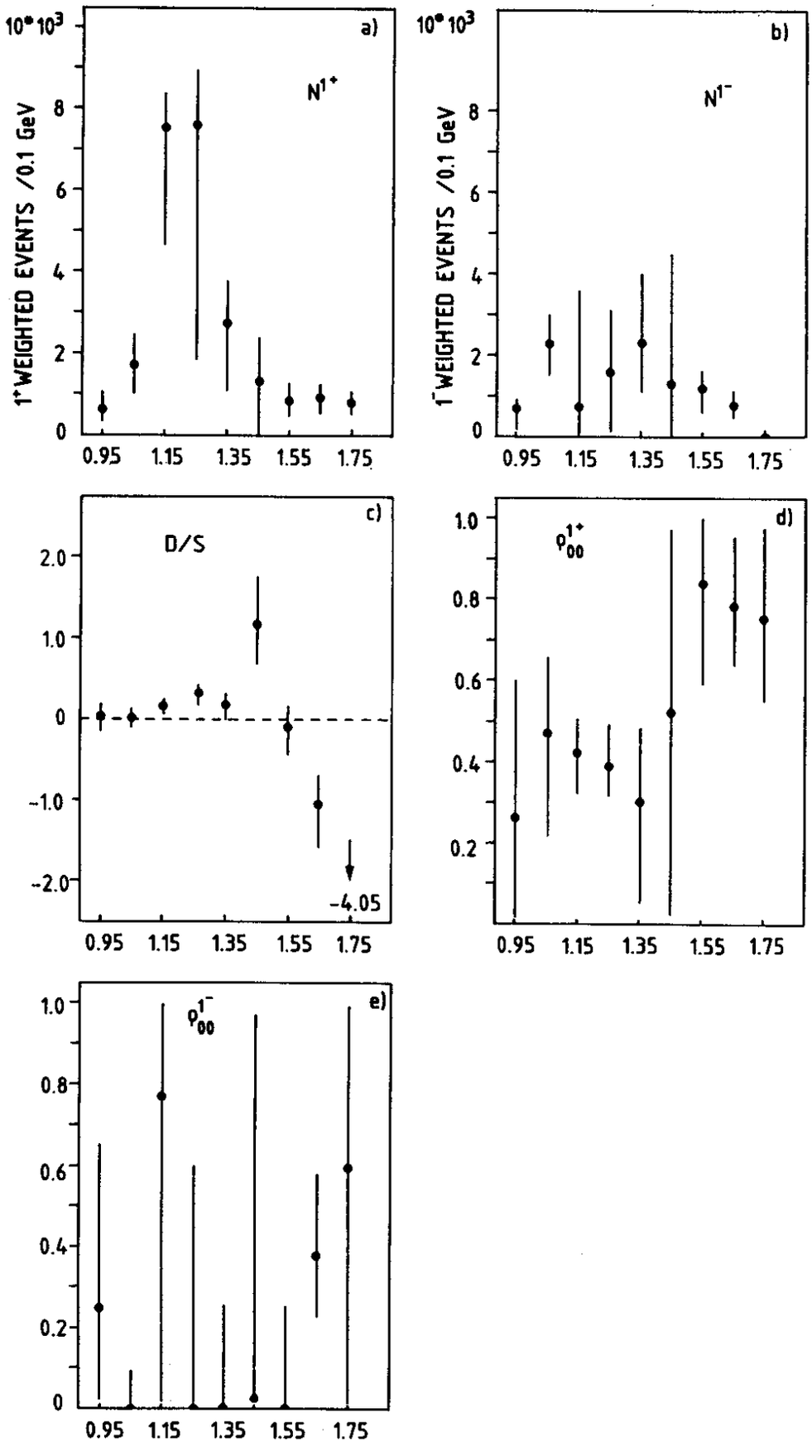
a)
$10^* 10^3$
1^+ WEIGHTED EVENTS /0.1 GeV
N^{1^+}
b)
$10^* 10^3$
1^- WEIGHTED EVENTS /0.1 GeV
N^{1^-}
c)
D/S
-4.05
d)
$\rho_{00}^{1^+}$
e)
$\rho_{00}^{1^-}$
0.95 1.15 1.35 1.55 1.75
$M_{\omega\pi^0}$ GeV

Fig. 11

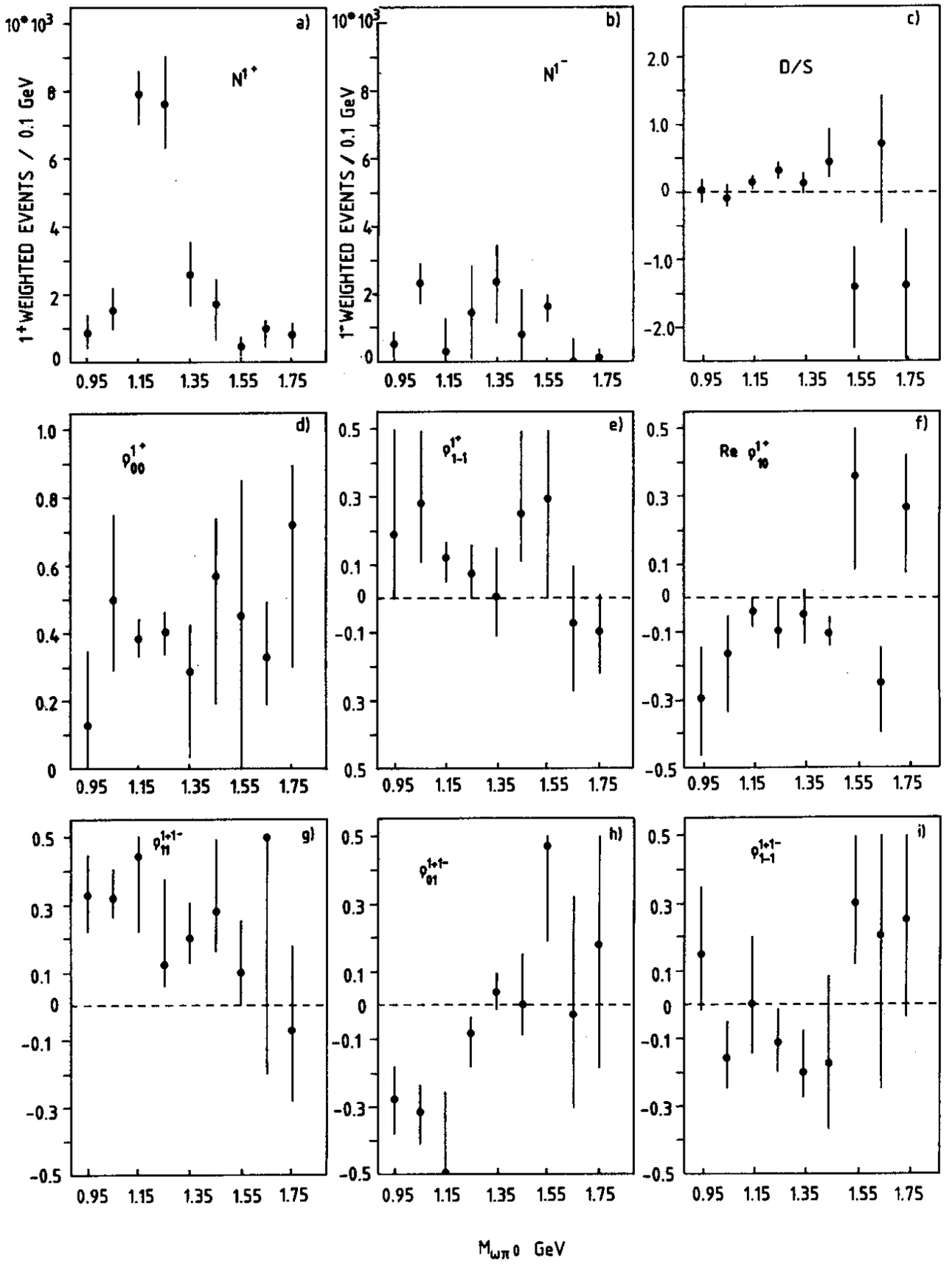
a)
N^{1^+}
$10^* 10^3$
1^+ WEIGHTED EVENTS / 0.1 GeV
b)
N^{1^-}
$10^* 10^3$
1^- WEIGHTED EVENTS / 0.1 GeV
c)
D/S
d)
$\rho_{00}^{1^+}$
e)
$\rho_{1-1}^{1^+}$
f)
Re $\rho_{10}^{1^+}$
g)
ρ_{11}^{1+1-}
h)
ρ_{01}^{1+1-}
i)
ρ_{1-1}^{1+1-}
0.95 1.15 1.35 1.55 1.75
$M_{\omega\pi^0}$ GeV

Fig. 12

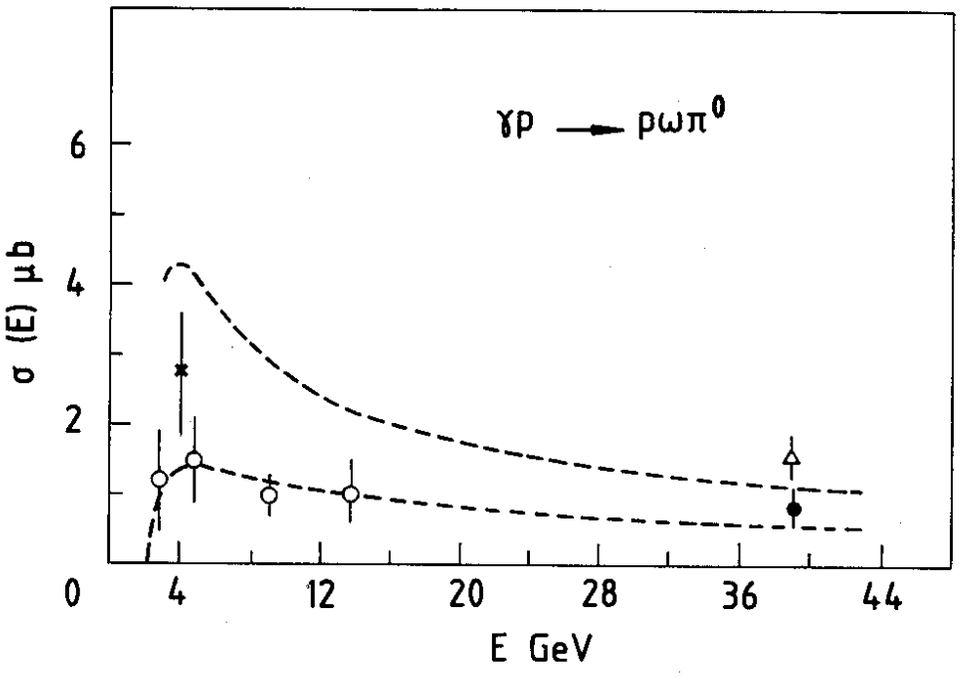

○ Ballam et al. [4] and refs therein.

---● This experiment

△ Aston et al. [5]

× Barber et al. [5]

Fig. 13